International Journal of Solids and Structures 51 (2014) 3996–4014

Contents lists available at ScienceDirect

International Journal of Solids and Structures

journal homepage: www.elsevier.com/locate/ijsolstr

Mechanics of the implosion of cylindrical shells in a confining tube

Sachin Gupta [a], James M. LeBlanc [b], Arun Shukla [a,*]

[a] Dynamic Photo Mechanics Laboratory, Department of Mechanical, Industrial and Systems Engineering, University of Rhode Island, Kingston, RI 02881, United States
[b] Naval Undersea Warfare Center (Division Newport), Newport, RI 02841, United States

ARTICLE INFO

Article history:
Received 4 March 2014
Received in revised form 15 July 2014
Available online 2 August 2014

Keywords:
Implosion
Implodable volume
Collapse
Pressure waves
Computational modeling
Fluid structure interaction
Water hammer
Confined environment

ABSTRACT

A fundamental experimental investigation, with corresponding computational simulations, was conducted to understand the physical mechanisms of implosions of cylindrical shells occurring within a tubular confining space which has a limited potential energy reservoir. In particular, attention was focused on studying the generation of pressure waves from the implosion, the interaction of the pressure waves with the confining tube walls and end caps, and the collapse mechanisms of the implodable volume. Experiments were conducted with three implodable volume geometries which had similar critical collapse pressures. The implodable volumes were aluminum 6061-T6 cylindrical tubing and were placed concentrically within the confining tube. Pressure histories recorded along the length of the confining tube during the experiments were utilized to analytically evaluate the deformation of the implodable volume using fluid–structure coupled deformation models. Computational simulations were conducted using a coupled Eulerian–Lagrangian scheme to explicitly model the implosion process of the tubes along with the resulting compressible fluid flow. The numerical model developed in this study is shown to have high correlation with the experimental results and will serve as a predictive tool for the simulation of the implosion of different cylindrical geometries as well as various tube-in-tube implosion configurations. The experimental results show that the limited hydrostatic potential energy available in a confined environment, as compared to a free field, significantly influences the implosion process. The wall velocities of the implodable volume during the collapse, as well as the extent of the collapse progression, are largely affected by the sudden decrease in the available hydrostatic potential energy. This energy is shown to be partially transformed into elasto-plastic strain energy absorbed in the deformation of the implodable volume, as well as the kinetic energy of the water during the implosion process. Experiments also show that the extent of the collapse progression of an implodable volume can potentially be inhibited within a closed environment, which can lead to the arresting of an implosion event prior to completion for larger implodable volumes. The pressure waves generated during collapse comprise of waves emitted due to the impact of the implodable volume walls, the arrest of rushing water and contact propagation along the walls. These processes later evolve into water hammer type axial wave behavior.

1. Introduction

A comprehensive series of experiments were conducted to study the mechanics of the implosion of cylindrical shells (implodable volume) in a tubular confining space. The emphasis was on understanding the physical mechanisms of implosion of cylindrical shells occurring within a confining space with limited potential energy reservoir. The implodable volumes consisted of aluminum 6061-T6 cylindrical tubing, and were placed concentrically and longitudinally centered within the confining tube. The collapse pressure was held approximately constant throughout the study. The pressure histories generated by the implosion event were captured by dynamic pressure transducers mounted on the inner surface of the confining tube.

Understanding the fundamental mechanisms associated with the implosion process has been a topic of interest since the early 1950's, especially in the marine pipelines and naval communities (Isaacs and Maxwell, 1952; Palmer and Martin, 1975; Turner, 2007; Urick, 1963). Typical examples of implodable volumes include deep ocean submersibles, submarines, underwater remote operated vehicles, underwater pipelines, and underwater sensors (Turner and Ambrico, 2012). An implodable volume can be defined as any structural shell or body that is acted upon by external pressure and contains internal gas at a lower pressure (or vacuum). In simple terms, the implosion of a structure can be understood as

* Corresponding author. Tel.: +1 401 874 2283; fax: +1 401 874 2355.
E-mail address: shuklaa@egr.uri.edu (A. Shukla).

http://dx.doi.org/10.1016/j.ijsolstr.2014.07.022
0020-7683/

a sudden loss of stability due to a net external force causing the structure to collapse onto itself. The resulting collapse of the structure is violent and results in rapid release of energy in the form of shock pressure waves, high velocity fluid motion, and sound (LeBlanc et al., 2014). An axial/lateral loading, uniform hydrostatic pressure or a combination of both can be the initiating and driving forces for the implosion of a structure. In underwater environments, this collapse is a dynamic process with duration of the order of milliseconds. At the onset of collapse, the implodable volume walls gain inwards momentum and the surrounding water rushes in to fill the resulting void generated in the collapse process. The fast inward traveling water surrounding the receding walls of a collapsing structure stops suddenly when the walls come into contact. However, the acquired momentum of the in-rushing water causes it to over-compress against the structure and produces strong outwardly radiating shockwaves. Such pressure pulses/shock waves can be large enough to potentially damage or even lead to the implosion of adjacent structures (Diwan et al., 2012; Farhat et al., 2013; Harben and Boro, 2001; Ikeda, 2012; Ling et al., 2013; Orr and Schoenberg, 1976; Turner and Ambrico, 2012; Vath and Colletti, 1968). A classical example of such an event is the 2001 accident at the Super-Kamiokande facility in Japan, where about 7000 photomultiplier tubes were destroyed by a sympathetic implosion event (Cartlidge, 2001).

In the past, many researchers have theoretically investigated the buckling of cylindrical shells to predict the critical hydrostatic collapse pressures (Timoshenko and Gere, 1963; Von Mises, 1929). The effect of imperfections and various defects has been presented in several research articles (Budiansky and Hutchinson, 1966; Simitses, 1986). It was concluded that the initial ovality of the cylindrical shell can significantly reduce the collapse pressure, while the variation in wall thickness has a minimal effect on the collapse pressure (Kyriakides and Corona, 2007). The propagation of buckles in offshore pipelines has also been widely studied (Charter et al., 1983; Kyriakides and Babcock, 1981; Kyriakides and Netto, 2000; Mesloh et al., 1973; Palmer and Martin, 1975).

Although the problem of buckling has been extensively investigated from the structural point of view, there have been very few studies reported which aim to understand the fluid motion and pressure wave emissions during underwater buckling of structures. In the early 1900's, Rayleigh (1917) developed analytical expression for the collapse of a spherical bubble inside an incompressible fluid. According to this theory, a pressure difference between the bubble and ambient internal pressure causes the bubble to collapse or grow, which results in an oscillatory bubble pulse. In the problem of a closed structure imploding in an underwater environment, the low pressure gas is contained inside a structure. Due to this fact, this structure plays a key role during the collapse process and the complex fluid–structure interaction between the structure and water governs the dynamics of the implosion. In the early 1960's, the implosion of glass spheres was used to generate acoustic signals for underwater applications (Isaacs and Maxwell, 1952; Urick, 1963). Orr and Schoenberg conducted implosion experiments using pre-weakened glass spheres (by grinding a flat spot) in the ocean and concluded that the implosion depth is dependent on the thickness of the flat spot (Orr and Schoenberg, 1976). Harben and Boro conducted implosion experiments with five glass spheres bundled together for boosting the amount of implosion energy released (Harben and Boro, 2001). Turner conducted near-field pressure measurements during the implosion of glass spheres and concluded that the failure time history of the structure has a significant influence on an implosion pressure pulse (Turner, 2007). Recently, Turner and Ambrico (2012) and Farhat et al. (2013) studied the implosion of aluminum cylindrical tubes. Turner and Ambrico (2012) concluded that there are four primary features of the implosion process in metal tubes: (1) the initial collapse phase, prior to wall contact, is accompanied by a smooth decrease in pressure in the surrounding water, (2) at the moment that contact is made between opposing sides of the collapsing cylinder at the center, a short duration pressure spike is emitted in the surrounding water, (3) a large positive pressure is produced at the instant that contact between the two opposing sides extends the full width of the cylinder, and (4) as the buckle propagates toward the ends, the pressure pulse continues, but at a lower magnitude, until the buckle reaches the end cap and the collapse of the cylinder completes. Farhat et al. (2013) extended this implosion work by studying both mode-2 and mode-4 collapse of aluminum cylindrical shells and demonstrated that the pressure pulse generated is influenced by the mode of buckling as well as the associated localization of collapse.

With advances in computational computing resources and efficiency, the modeling and simulation of implosion phenomenon has gained interest. Early numerical studies involving underwater implosions generally represented the implodable volume as a gas bubble within a high pressure fluid field. Kadioglu and Sussman (2008) utilized an adaptive solution methodology to solve the multi-phase problem of a gas bubble contained within a water field. Farhat et al. (2008) simulated the 2 phase flow problem with a solution methodology known as the "ghost fluid method for the poor" (GFMP). The work extended the original GFMP method to better handle the large discontinuities of pressure and density at the air/water interfaces. These studies have generally focused on the two-phase nature of the fluid flow but have neglected the fluid structure interaction which has been shown to be important in the implosion of a structural body. Turner (2007) utilized the coupled Eulerian–Lagrangian fluid structure interaction code (Dynamic System Mechanics Analysis Simulation code or DYSMAS) to simulate the collapse of glass spheres to determine the influence of the failure rate of the spheres on the resulting pressure histories. The primary conclusion was that a computational model of an underwater implosion event must include the structure that separates the low pressure air from the high pressure water. If the structure is neglected, the model would over predict the peak pressure generated from the collapse. Turner and Ambrico (2012) also utilized the DYSMAS code to simulate the implosion of metallic cylindrical bodies. Farhat et al. (2013) investigated the pressure pulses resulting from an implosion, and the parameters which influence the nature of the pulses, through the AERO software suite. The simulations were shown to accurately capture both the deformations of the structure as well as the pressure waves resulting from the collapse. Recently, Chamberlin and Guzas (2012) developed energy metrics to characterize underwater implosion and used these metrics to examine the energy balance during an implosion event. For a series of test cases involving hydrostatic implosion of ductile metal cylinders, they found that the structure absorbs the majority of the initial energy of the system and the released pressure pulse carries away a small percentage of the initial energy Chamberlin and Guzas (2012).

All these experimental and numerical studies on implosion mentioned above were conducted in a free-field environment, where the net hydrostatic pressure in the surrounding fluid is maintained during the implosion process and the free-field environment acts as an infinite source of hydrostatic potential energy to drive the implosion process. On contrary, in the case of implosion occurring within a confining space, the source of hydrostatic potential energy to progress the implosion is limited. Hence, the ratio of energy required to deform the implodable volume and the initial potential energy available acts as a critical factor to drive the implosion process. Costa and Turner (2008) did study the implosion of a tube occurring within an open-ended confining tube and showed that the implosion phenomenon significantly differs from a free-field implosion, however, due to open ended nature

of their confining tube, infinite energy was still available for driving the implosion process. Such implosions have shown to be capable of generating strong hammer pressure waves (up to 5 times of the collapse pressure) at the closed end of the confining tube, which is highly detrimental to the nearby structures. Another study on understanding the implosion of structures in a confining space was performed by Bitter and Shepherd (2014). They studied the dynamic buckling of submerged tubular structures in a closed tube. Tube buckling experiments were performed by applying impulsive loading in the water filled outer tube and dynamic buckling theoretical models were developed involving the fluid structure interaction. In their experiments, the dynamic impulse loading applied was an order of magnitude higher than the critical buckling load, therefore the dynamic impulsive loading was only considered to cause the implosion and the effect of initial hydrostatic pressure was not investigated.

The primary objective of this study is to understand the mechanics of implosion of cylindrical shells inside a closed confining tube. The experiments conducted with a range of d/D (diameter of implodable/diameter of the confining tube) cylindrical shells revealed that the limited hydrostatic energy available in the confined environment significantly influences the implosion process. The extent of collapse and the velocity of the implodable walls are smaller for large diameter cylindrical shells, although the change in internal volume of the implodable is relatively similar for all shells.

2. Experimental setup

A schematic of the experimental setup for the tubular confined space implosion facility is shown in Fig. 1. It consists of a confining tube mounted on a horizontal I-beam section and an inner tube (implodable, shown in Fig. 2). The confining tube is made out of seamless low-carbon steel (SA106-B) pipe with the specifications from pressure vessel handbook (Buthod, 1983) and has an inner diameter of 177.8 mm (7 in) with 19 mm (0.75 in) wall thickness. The overall length of the confining tube is 2.13 m (84 in). The high frequency dynamic pressure transducers (PCB-113B22) are installed in the wall of the vessel such that the sensor element is flush with the inner surface. The dynamic pressure transducers have a rise time of <1 μs, resolution of 0.14 kPa (0.02 psi) and high resonant frequency (>500 kHz). The transducers are placed along a single line axially in the confining tube, and the distance between the sensors varies between 76 mm (3 in) to 305 mm (12 in) depending on their axial position (see Fig. 1 for exact locations). Three sensors are placed in the close vicinity of the center of the confining tube to exclusively capture the fluid pressure drop with the collapse progression in the implodable. A data acquisition system with 200 kHz bandwidth is used to capture the dynamic pressure history in the confining tube at a sampling rate of 2 MHz. Additionally, a static sensor is installed to monitor the hydrostatic gage pressure of the confining tube before the implosion occurs. The confining tube is inclined at an angle of $\sim 2^\circ$ at one end manually in order to remove the excess air present in the confining tube to the maximum extent possible before pressurization.

The implodables used in this study are made out of commercially available aluminum 6061-T6 extruded seamless tubing. Table 1 gives a brief layout of the experiments conducted in this study. The diameter of the implodable volume is increased from 31.8 mm (1.25 in) to 50.8 mm (2 in) to 76.2 mm (3 in) to increase the ratio of implodable diameter (d) to the confining tube diameter

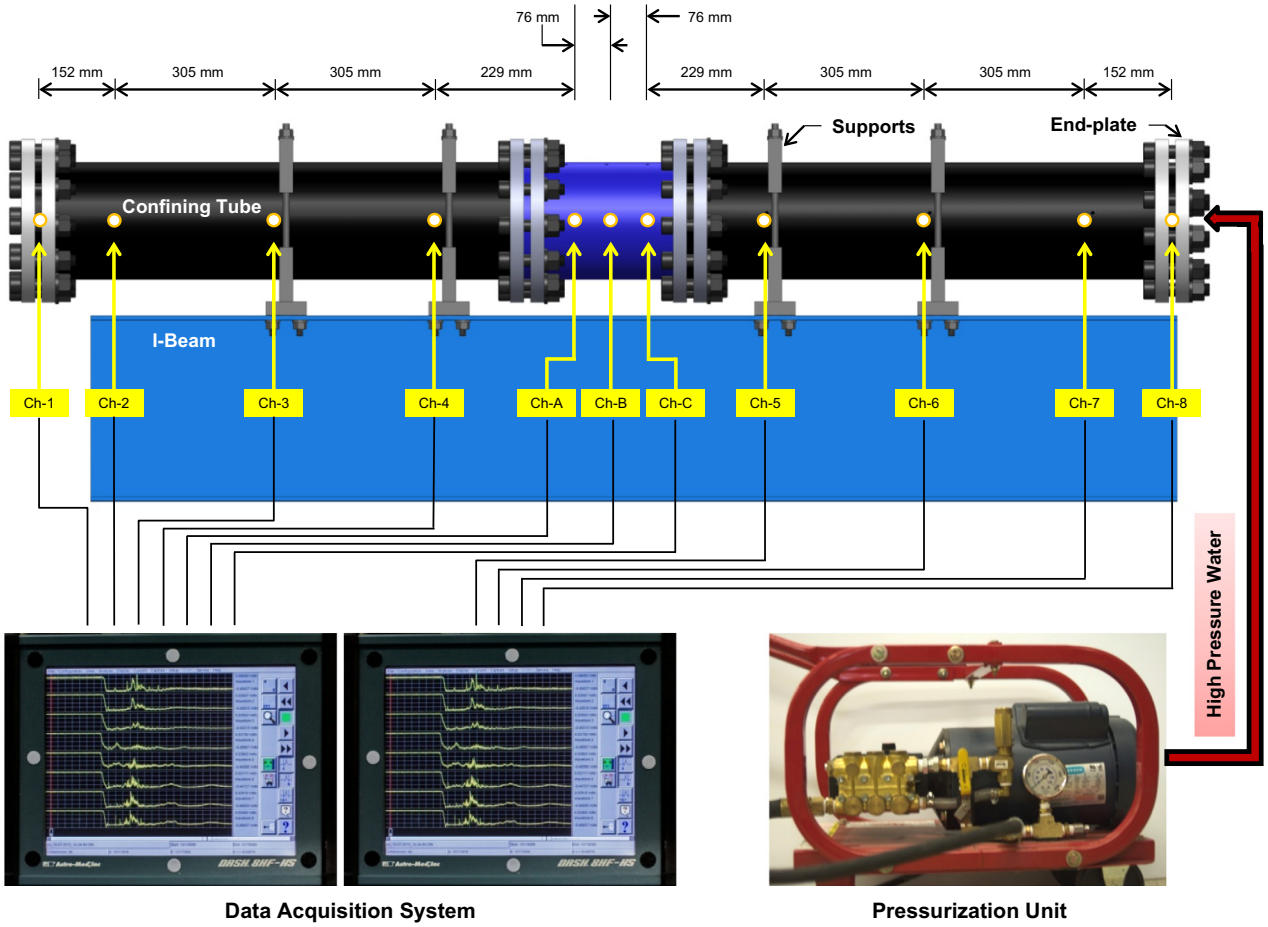

Fig. 1. Schematic of experimental setup.

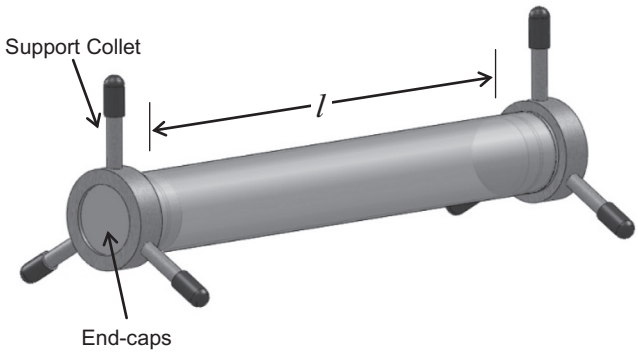

Fig. 2. Schematic of implodable volume.

(D). The unsupported length (l) of the implodables is fixed at 304.8 mm (12 in) and the wall thickness (h) is increased to keep the critical buckling pressure approximately constant. The increasing implodable diameter allows for a large range of the ratio between the confining space's volume and implodable's volume (from ~30 to 200). A schematic of the mounting fixture for holding the implodable is shown in Fig. 2. The implodables are sealed on both ends using solid aluminum end-caps, which utilize circumferential o-rings for sealing the specimen for underwater experiments. This tube and end-cap assembly is mounted inside the confining tube using support collets, which ensure concentric placement of the implodable in the confining tube. The construction of the three spoke collet is chosen so as to provide minimal interference to the axial pressure waves and water flow within the confining tube during the implosion event. The effect of initial ovality and wall thickness variation on the critical buckling pressure has been widely reported (Kyriakides and Corona, 2007). Therefore, ovality parameter $(\Delta_0 = (D_{max} - D_{min})/(D_{max} + D_{min}))$ and wall eccentricity parameter $(\Xi_0 = (h_{max} - h_{min})/(h_{max} + h_{min}))$ are measured for each specimen to quantify the initial imperfections present in the specimen before experiments and are shown in Table 2.

The confining tube is filled and pressurized with water using a hydrostatic pump. The pressurization rate during the experiments is kept at 0.689 MPa/min (100 psi/min). This ensures a negligible increase of pressure ($\sim 10^{-5}$ MPa) during the typical implosion event (<2 ms). When the implodable reaches the critical buckling pressure, the implosion occurs and generates an audible noise. This noise is utilized as a signal to manually shut down the hydrostatic pump. Due to the relatively small flow rate of the hydrostatic pump (0.0935 ml/ms), the external water flow during the implosion event from outside in the confining tube can be neglected in the transient pressure time histories.

3. Computational model

Computational models of the implosion experiments are developed using the Dynamic System Mechanics Analysis Simulation (DYSMAS) software, maintained by the Naval Surface Warfare Center (NSWC), Indian Head Division. The software is a fluid–structure interaction (FSI) code that consists of structural solver (ParaDyn), a fluid solver (GEMINI), and the standard coupler interface. ParaDyn is an explicit Lagrangian solver suitable for large deformation dynamic problems. GEMINI is an explicit Eulerian fluid solver with equation of state (EOS) models for gases, liquids, explosives, and solids. The standard coupler interface allows the fluid and structural codes to share the required variables for the fluid structure interaction problem.

The computational models are developed to (1) capture the fluid structure interaction between the implodable and the surrounding fluid, (2) predict the pressure time history resulting from the implosion and, (3) predict the final collapsed shape of the implodable. The models include the implodable, the air contained within the implodable, the high pressure water contained between the implodable and the confining tube, the confining tube itself, and a small entrapped air bubble along the top edge of the confining tube.

Table 2
Ovality parameter and wall eccentricity for all geometries.

Geometry no.	Ovality parameter (Δ_0) (%)	Wall eccentricity (Ξ_0) (%)
1	0.04	1.41
2	0.06	0.97
3	0.07	2.21

3.1. Structural model

The structural model, Fig. 3, consists of the implodable, confining tube and a mechanical indenter. The model is a one-quarter symmetry model consisting of symmetry planes oriented such that the model represents one-half of the length and one-half of the circumference of both tubes. Although the 31.8 mm and 50.8 mm diameter implodables collapse in a pure mode-2 shape which is 1/8 symmetric, the 76.2 mm implodable only exhibits 1/4 symmetry collapse and thus 1/4 symmetric models are used for consistency. The indenter is only part of the computational model and is not present in the actual experiment and is needed to initiate the collapse at the same pressure as seen in the experiments. The wall thickness variations and ovality imperfections in the implodables are not accounted for in the numerical model. Therefore the model is inherently stronger than the actual implodable and must be numerically initiated to correspond to the experiments.

Both the implodable and the confining tube are modeled with 80 quadrilateral shell elements around half the circumference and 200 elements along one-half on the length. This results in element sizes on the order of 0.6 mm for the implodable and 5 mm for the confining tube. Although the confining tube consists of larger elements, it is assumed to be sufficiently rigid due to its thickness such that deformations are minimal and the larger elements are acceptable. All structural elements utilize the Hughes-Liu element formulation with 5 integration points through the thickness of the elements. The outer surface of the implodable and the inner surface of the confining tube are modeled with appropriate shell offsets so as to capture the correct locations of the wetted surfaces. The steel confining tube is modeled as a linear isotropic material and the aluminum implodable is modeled with a "Rate-Dependent

Table 1
Layout of the experiments.

Geometry no.	Wall thickness (h)	Outer diameter (d)	Internal volume (V_1)	$V_1/V_{confining\ tube}$	l/d	d/h	Experimental collapse pressure (P_c)
1	0.89 mm (0.035 in)	31.8 mm (1.25 in)	241 ml	1/187.5	9.6	35.7	4.14 MPa (600 psi)
2	1.24 mm (0.049 in)	50.8 mm (2.00 in)	616 ml	1/73.05	6	40.8	3.33 MPa (484 psi)
3	1.65 mm (0.065 in)	76.2 mm (3.00 in)	1386 ml	1/32.47	4	46.2	3.59 MPa (520 psi)

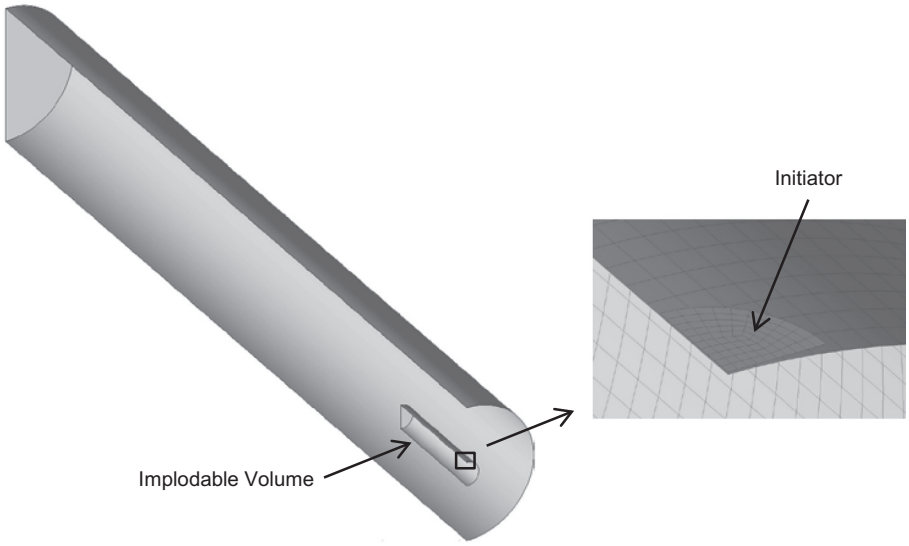

Fig. 3. Structural model of confining tube and implodable volume.

Tabular Isotropic Elastic–Plastic" material model, although rate dependency is not considered in the current model.

3.2. Fluid model

The fluid model consists of the air internal to the implodable, the high pressure water contained within the confining tube, a small entrained air bubble at the top of the fluid body, and low pressure air external to the confining tube (see Fig. 4). The initial entrapped air bubble in the system is included due to the inability to fully evacuate all of the air from the confining tube in the experiments due to the horizontal orientation. The difference in pressures between the high pressure water and the ambient air contained within the implodable corresponds to the collapse pressure observed during the experiments and is unique to each geometry. Since the hydrostatic pressure recorded during the experiments is actually the gage pressure and not the absolute pressure in the fluid, the fluid pressure in the simulations corresponds to the observed collapse pressure plus the atmospheric pressure. By applying atmospheric pressure to the air inside the implodable, the same net pressure differential (collapse pressure) is achieved. For all geometries, the same fluid grid is utilized for consistency. The grid has fluid cell sizes of 0.75 mm in way of the implodable itself with the cells tapering to 1.5 mm in the radial direction towards the confining tube, and tapering to 2.5 mm in the axial direction towards the confining tube end-plates. In order to accurately capture the relatively small size of the bubble at the top of the confining tube, the cell size is refined to 0.2 mm at this location in the vertical direction. The fluid grid has a total of 20.8 million fluid cells. The air is modeled using an adiabatic, isentropic equation of state and the water is modeled with the compressible Tillotson equation of state. The sides of the grid that correspond to symmetry planes have fixed reflecting boundary conditions and the other sides have free non-reflecting conditions.

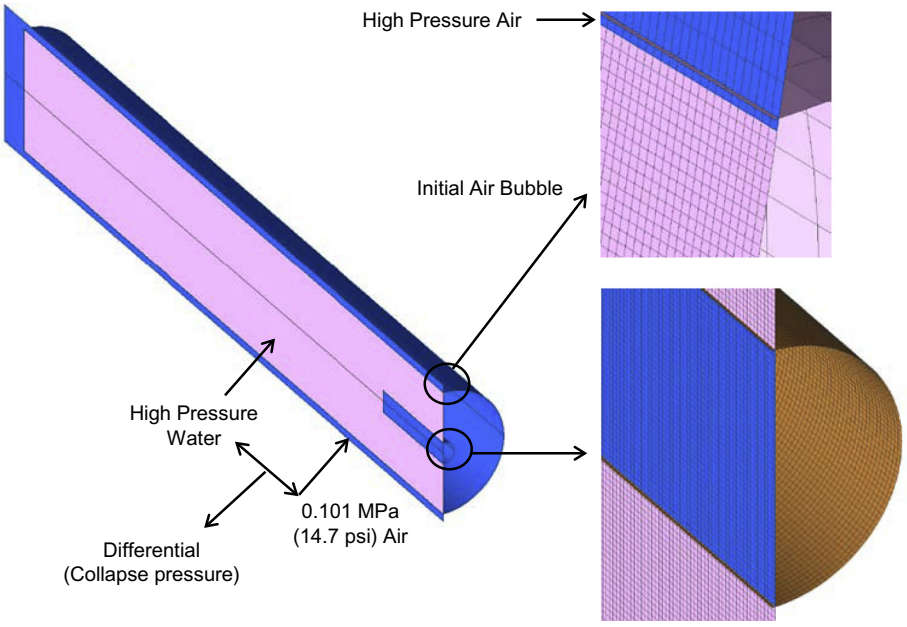

Fig. 4. Fluid model of air inside the implodable volume, high pressure water inside the confining tube and initial entrapped air bubble.

3.3. Complete DYSMAS model

In the computational models, the fluid and structural meshes are coupled through the use of interface element definitions which define the "wetted surface" of the structure. In the current models, doubly wetted interface elements are used in which fluid (water/air) can act on both faces of the shell elements. This is an important consideration since both the implodable and confining tube interface with both air and water. As these interface elements move through the fluid domain during the collapse of the implodable volume, air cells that are initially contained within the implodable body can transition to water cells. The indenter is not included in the fluid structure interaction definition as the collapse has been initiated prior to the fully coupled run.

3.4. Loading/collapse initiation

In the computational models, the hydrostatic loading and subsequent collapse initiation are comprised of a two step process which occurs in an uncoupled preload simulation for computational efficiency. In the first step of the preload process, the cylindrical shell is hydrostatically loaded to the collapse pressure (gage pressure) observed in the respective experiments through a dynamic relaxation procedure in which the pressures are applied to the segment faces defining the water side surfaces of the implodable and confining tube. Once the dynamic relaxation phase converged, the cylindrical shell is squeezed upon by a radially inward moving indenter at a velocity of 60 cm/s. During this indentation phase, the position of the implodable's wall in way of the indenter is monitored until the wall separates from the indenter, which indicates the initiation of the collapse. At this point in time, the simulation is terminated and a file containing the relevant structural quantities (i.e. stresses, position, velocities) is written. This file is then used as the starting point for the structural component of the fully coupled DYSMAS simulation. It must be noted that for the fully coupled run, the mechanical pressures applied in the preload model are removed since the hydrostatic load is applied through coupling with the fluid domain in the coupled simulation. This process greatly reduces the computational resources needed to preload and initiate the collapse of the model. Although the same process could be applied in a fully coupled run, the computational time (cpu hours) would be greatly increased due to the fluid domain cost which is not required during this phase of the model loading.

4. Results and discussion

4.1. Experimental results

The pressure profiles generated from the implosion of cylindrical shells inside the confining tube are captured for the experiments conducted on 31.8 mm, 50.8 mm and 76.2 mm outer diameter implodable volumes. These pressure histories are analyzed in detail in order to understand the mechanics of deformation of the implodables during the collapse. In subsequent sections, the analytical approaches in conjunction with experimentally observed pressure histories are utilized to predict the fluid motion inside the confining tube during the implosion. The energy redistribution of the initial hydrostatic potential energy is also discussed to distinguish between a rapid and a slow buckling process.

4.1.1. Evolution of pressure waves inside the confining tube

Underwater buckling of an implodable generates sudden dynamic deformation in the implodable walls, causing rapid motion and decrease in dynamic pressure in the surrounding fluid. This dynamic pressure drop causes development of low pressure waves. Similarly in the case of the implosion inside a confining tube, low pressure waves are emitted from the center of the implodable (or the center of the confining tube). These low pressure waves travel outwards in both axial directions towards the ends of the confining tube. Such pressure waves travel at a coupled pressure wave speed, which has been widely studied in water hammer theory. Early studies by Korteweg (1878) and Joukowsky (1900) have shown that the radial oscillation of a fluid filled tube is coupled with the longitudinal (axial) motion of the fluid and the coupled longitudinal pressure wave speed (c_f) in the fluid is given by

$$c_f = \frac{c}{\sqrt{1+\frac{2KR}{Eh}}} \tag{1}$$

where the parameters are listed in Table 3.

Recent investigation by Tijsseling (2007) estimated the coupled longitudinal pressure wave speed (c_f) in a fluid filled thick walled tube, which is given by

$$c_f = \left\{\rho_f\left[\frac{1}{K}+\frac{2}{E}\left(\frac{R}{h}\left(1-\frac{v^2}{1+h/2R}\right)+\frac{1+h/R}{2+h/R}+v\right)\right]\right\}^{-1/2} \tag{2}$$

For the case of the confining tube geometry chosen in this study, both Korteweg's and Tijsseling's theory predict that the coupled longitudinal pressure wave speed to be 1395 m/s. As the inner diameter of the confining tube (177.8 mm) and the unsupported length of the implodable (304.8 mm) are of the same order, the nature of the pressure waves in the vicinity of the implodable is approximately radial. Therefore, for the experimental determination of the pressure wave speed near the specimen, a spherical pressure wave front emission from the central part of the implodable is assumed as shown in Fig. 5(a). The path difference for the arrival of the pressure wave at each nearby transducer location was calculated by geometry as shown in Fig. 5(b).

In Fig. 5(b), points *B* and *C* represent the location of transducers ch-B and ch-C in the confining tube. The pressure wave front is generated from point *A* of the implodable wall surface and reaches points *B* and *M* simultaneously. Therefore, in order to reach point*C*, the pressure wave needs to travel distance*MC*, which can be calculated as,

$$MC = AC - AM = \left[\left[\frac{1}{2}(D-d)\right]^2 + l_1^2\right]^{1/2} - \frac{1}{2}(D-d) \tag{3}$$

Table 4 shows the values of path difference (MC) between ch-B and ch-C for different geometries. The larger diameter implodable has greater path differences (relatively closer to l_1), which suggests an axial approximation near implodable is more accurate for larger implodables.

The path differences between the transducers away from the implodable (i.e. Ch-1 to 4, Ch-5 to 8) was taken as their axial locations' difference as the radial nature of pressure waves can

Table 3
Properties of the confining tube material and water.

Parameter	Value
ρ_f(density of water)	998.85 kg/m^3
K (bulk modulus of water)	2.149 GPa
c (wave speed in water)	1467 m/s
R (inner radius of the tube)	88.9 mm (7.00 in)
E (elastic modulus of the tube material, SA106-B steel)	210 GPa
v (Poisson's ratio)	0.29
h (thickness of tube wall)	19 mm (0.75 in)
L (length of the tube)	2.13 m (84 in)

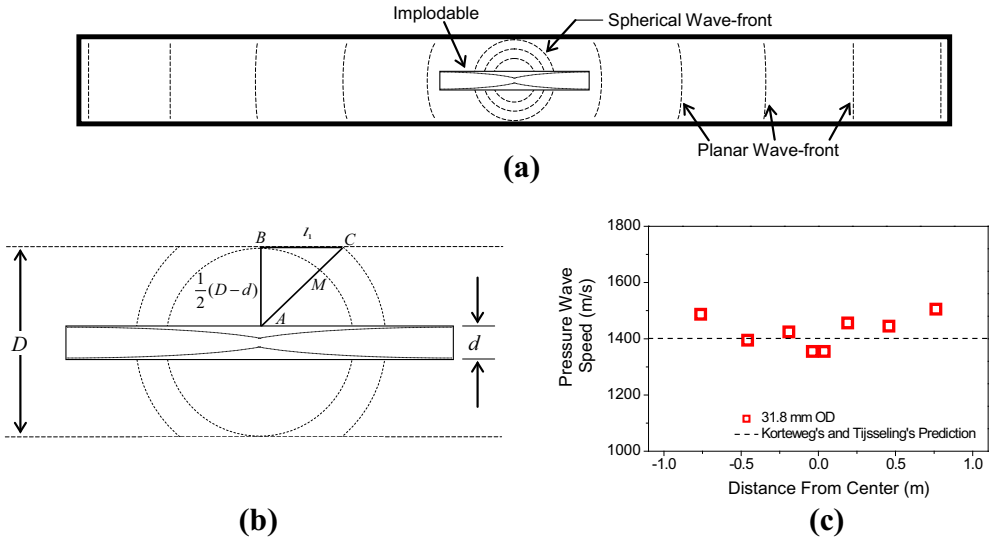

Fig. 5. Longitudinal pressure wave velocity estimation in the confining tube. (a) initial pressure wave development in the confining tube, (b) path difference calculation between ch-B and ch-C, and (c) longitudinal pressure wave velocity for 31.8 mm OD (geometry 1).

Table 4
Path difference (MC) between ch-B and C for all geometries.

Geometry no.	Outer diameter (d)	l_1	MC
1	31.8 mm (1.25 in)	76.2 mm (3.00 in)	32.5 mm (1.28 in)
2	50.8 mm (2.00 in)	76.2 mm (3.00 in)	35.7 mm (1.41 in)
3	76.2 mm (3.00 in)	76.2 mm (3.00 in)	40.8 mm (1.61 in)

be neglected beyond the implodable location (assuming the wave becomes planar after traveling two diameters away from the center). Using these path differences, the wave speed inside the confining tube is calculated by estimating the time difference between the arrivals of pressure wave front at each respective transducer location and is shown in Fig. 5(c). As it can be seen from Fig. 5(c), the speed is in good agreement (~5% error) with the Korteweg and Tijsseling predictions. It is important to note during this analysis the wave speed should be estimated before any reflected wave from the end-plates arrive at the transducer locations. Therefore, pressure wave velocity is estimated in the central half axial length of the confining tube, which receives reflections only after 0.7 ms duration.

4.1.2. Pressure history comparison

The pressure profiles observed in the confining tube for different geometries are shown in Fig. 6. Note that the pressure profiles observed in the implosion experiments exhibited symmetry, as the implodables are placed at the center of the confining tube. Time $t = 0$ is arbitrarily chosen prior to any dynamic pressure variations observed in the experiments. Each figure shows three pressure traces: (1) ch-B, which shows the pressure history at the center of the confining tube, (2) ch-6, which shows the pressure halfway between the implodable and the end-plate, and (3) ch-8, which shows the pressure history at the far end of the confining tube (end-plate). The ch-8 transducer is placed at center of the end plate whereas ch-B and 6 are flush mounted in the inner walls.

The theoretical critical buckling pressure calculated for the nominal dimensions of the geometry 1 using von-Mises theory is 3.72 MPa (540 psi) (Timoshenko and Gere, 1963; Von Mises, 1929), while during experiments the collapse occurs at 4.14 MPa (600 psi). Such critical pressure variation can be attributed to small difference in the mean wall thickness of the commercially received tube specimens from the nominal value.

As shown in Fig. 6, the initial decrease in the pressure at ch-B corresponds to the beginning of the collapse process. The buckling of the specimen occurs in mode-2 shape (two lobes) for geometry 1 and 2, while geometry 3 exhibits a single indentation only (this will be discussed later in Section 4.2). The buckling begins at the mid-span of the specimen, while the remaining specimen stays stationary. The initial buckling causes a local change in the volume of the specimen at the center. At the critical buckling pressure, there is some excess volume of water present in the confining tube with respect to atmospheric pressure conditions, which maintains the hydrostatic pressure inside. This "excess compressible water" has two components: (1) actual compressible water present at high pressure and (2) the elastic expansion of the confining tube causing increased volume of water inside. If initial volume of the implodable ($V_{implodable\_i}$) is assumed to be negligible as compared to confining tube volume ($V_{implodable\_i} \ll \pi R^2 L$), the volume of excess compressible water (V_{excess_water}) can be estimated as following,

$$V_{water\_i} = \pi R^2 L\left(1 + \frac{P_c R}{2hE}(5 - 4\nu)\right) - V_{implodable\_i} \tag{4}$$

$$\begin{aligned} V_{excess\_water} &= V_{water\_i}\left[1 + \frac{P_c}{K}\right] - \left(\pi R^2 L - V_{implodable\_i}\right) \\ &\approx \pi R^2 L\left(\frac{R}{2hE}(5 - 4\nu) + \frac{1}{K}\right)P_c \end{aligned} \tag{5}$$

where V_{water_i}= the initial volume of water at the critical buckling pressure (P_c).

In the rightmost expression in Eq. (5), the first term represents the elastic expansion of the confining tube and second term is due to the compressibility of water. For the case of geometry 1, Eq. (5) shows that there is ~109 ml excess compressible water present in the confining tube and any comparable changes in the volume of the specimen with respect to 109 ml can decrease the overall hydrostatic pressure. In the case of geometry 1, it is observed that there is a rapid decrease of the pressure near the implodable, while the pressure near the end-plate remains constant. This decrease in the pressure of the fluid immediately surrounding the specimen is directly related to the inward velocity at which the shell surface is moving during the collapse. Therefore, during the buckling process, a pressure release wave in the surrounding water is emitted from specimen's wall. Initially, this wave propagates spherically

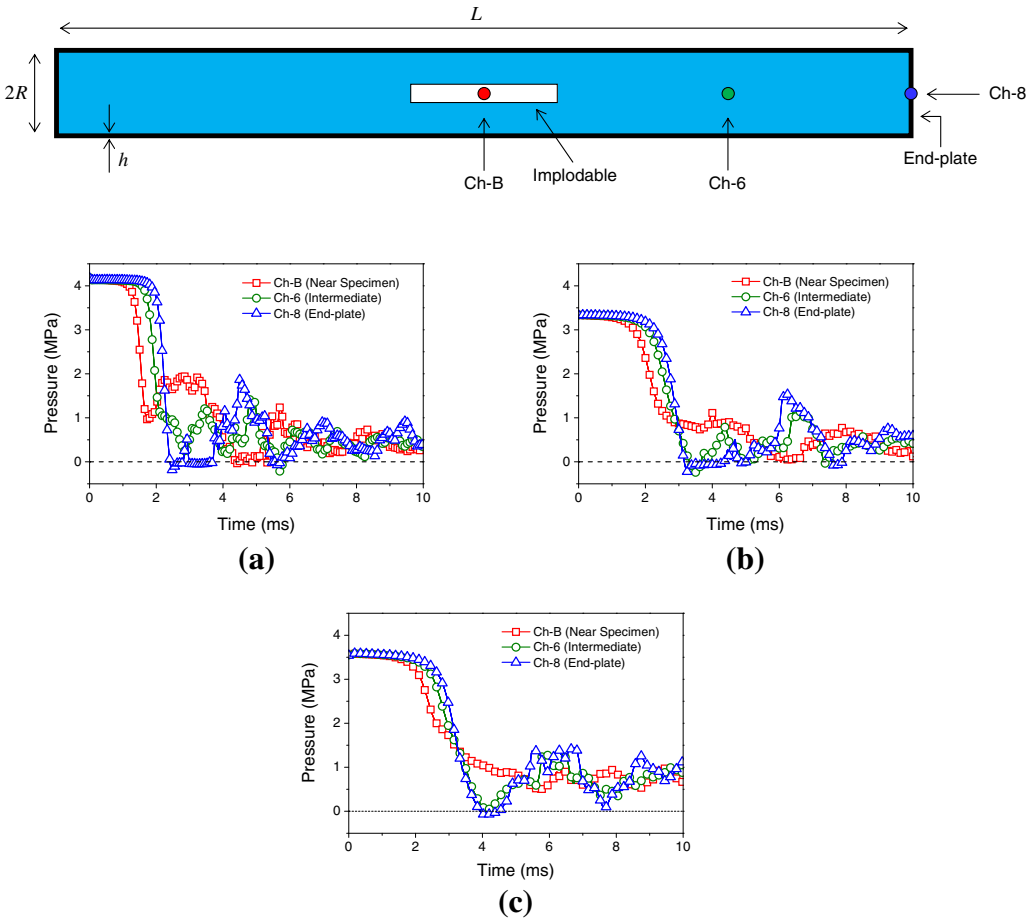

Fig. 6. Pressure history in confining tube. (a) 31.8 mm OD implodable (geometry 1), (b) 50.8 mm OD implodable (geometry 2), and (c) 76.2 mm OD implodable (geometry 3).

outwards and later axially towards the end-plate at coupled acoustic wave velocity causing the pressure to drop in the confining tube. These pressure release waves propagate the transient pressure disturbances in order to create spatially uniform hydrostatic pressure in the confining tube. For geometry 1 (see Fig. 5(a)), the initial pressure release wave emitted at $\sim t = 1.2$ ms reaches the end-plate at approximately $t = 1.9 \sim 2.0$ ms. It can be observed that the time scale of the pressure drop near the specimen ($\sim$0.6 ms) is smaller as compared to the 1/2 time period of the pressure wave oscillation in the confining tube ($\sim$1.5 ms). So, the release wave front emitted by the geometry 1 is a short wavelength pressure pulse traveling outwards in the confining tube and it does not overlap with itself at the center.

It is interesting to see that the pressure drop at the end-plate (ch-8) is larger than that experienced at the center (ch-B). In the initial pressure decay region, the pressure at the end-plate almost reaches zero. This phenomenon is similar to the reflection of a high pressure wave from a rigid wall in water (virtually incompressible fluid), where the pressure imparted on the rigid wall is twice the magnitude of the incident pressure (Taylor, 1963). From the classical acoustic shock wave theory for water (Taylor, 1963) and assuming rigid reflection of the wave from the end-plate, the pressure decay rate almost doubles in magnitude in this case and a sharp pressure drop at the end-plate is observed (the increase in decay rate at the end-plate is apparent by looking ahead to Fig. 12). It can also be seen that in the initial collapse process, the release pressure wave emitted at the center has the strength of almost 75% of the initial hydrostatic pressure; therefore the end-plate encounters twice the magnitude of the pressure wave ($\sim$150%). As a result, it causes a region of cavitation to develop at the end plate walls due to the inability of water to sustain tensile (negative) pressures. The presence of cavitation is indicated by the time duration of a zero pressure at the end-plate.

After the low pressure wave reflects from the end-plate, the net velocity of water still remains towards the center, which causes pressure to increase/maintain at the central region of the confining tube depending upon geometry. The resultant high-pressure waves reflect outward and eventually interface with the end-plates, which until this time had experienced zero pressure, as seen on transducers ch-1 and ch-8. These high pressure waves are similar to the classic water hammer wave studied in the opening/closing of valves in pipelines. In this case, the implosion of the specimen acts as *an opening of a check-valve* at the center of the confining tube, which develops a mean axial flow in the water towards the center. When the implosion process completes/arrests, the flow of water is restricted, representing *a sudden closing of a check-valve*, which is responsible for a high pressure hammer wave occurrence during these experiments. According to the water hammer theory, the time period of the hammer wave is $T = 4 \times (Length/Wave\ Speed)$ (Potter et al., 2002). Similarly in the case of the confining tube, the duration of the zero-pressure region can be written as,

$$T_{zero-pressure} \approx \frac{T}{2} = 2 \times \frac{Half\ Length\ of\ the\ Confining\ Tube}{Wave\ Speed\ in\ Water}$$
$$= 2 \times \frac{1.067\ \text{m}}{1395\ \text{m/s}} = 1.530\ \text{ms} \quad (6)$$

After the development of these high pressure waves, the behavior of pressure inside the confining tube stays oscillatory. A schematic of such high/low pressure wave generation is also shown in Fig. 7. Please note that the local radial flow of water near the center of the implodable is neglected in Fig. 7 and only the axial motion of water particles is shown for simplicity.

In the case of geometry 2 and 3, it is observed that the pressure drop at any location inside the confining tube is slower as compared to geometry 1 and decreases with increasing diameter (see Fig. 6(b) and (c)). Also in comparison to geometry 1, these geometries exhibit a relatively slower collapse and the collapse process was observed to lie between highly dynamic and quasi-static. As a result, the pressure waves have enough time to stabilize within the confining tube. The pressure near the specimen (ch-8) initially monotonically decays over time and does not exhibit any hump as observed in geometry 1.

In all the geometries, the onset of implosion generates low pressure acoustic waves from center. Later, further pressure drop at the center causes unsteady flow of water towards the implodable. The mechanism of the movement of water during initial collapse can be described as sink and source: (1) the end-plate region acts as a source of water, (2) the central region acts a sink of water. The net motion of water towards the implodable during the collapse process causes high pressure development at the center of the confining tube. This in turns leads to repeated high and low pressure wave oscillations after collapse finishes.

4.1.3. Wall contact and shock generation

Free field hydrostatic implosion of cylindrical shells have shown that the contact made between opposing sides at the center of a collapsing cylinder generates a shorter duration small pressure spike followed by a longer duration large pressure spike, which is produced at the instant that contact between the opposing sides extends the full width of the cylinder (Turner and Ambrico, 2012). These pressure spikes are locally generated from the implodable's surface and decay almost as a spherical wave as a function of 1/r. In the present study, such pressure spikes are also observed for geometry 1 (which exhibited full collapse/wall contact during experiments) and is shown in Fig. 8. At t = 1.99 ms in Fig. 8, a sharp pressure spike with a rise time of 5 μs is observed at ch-B

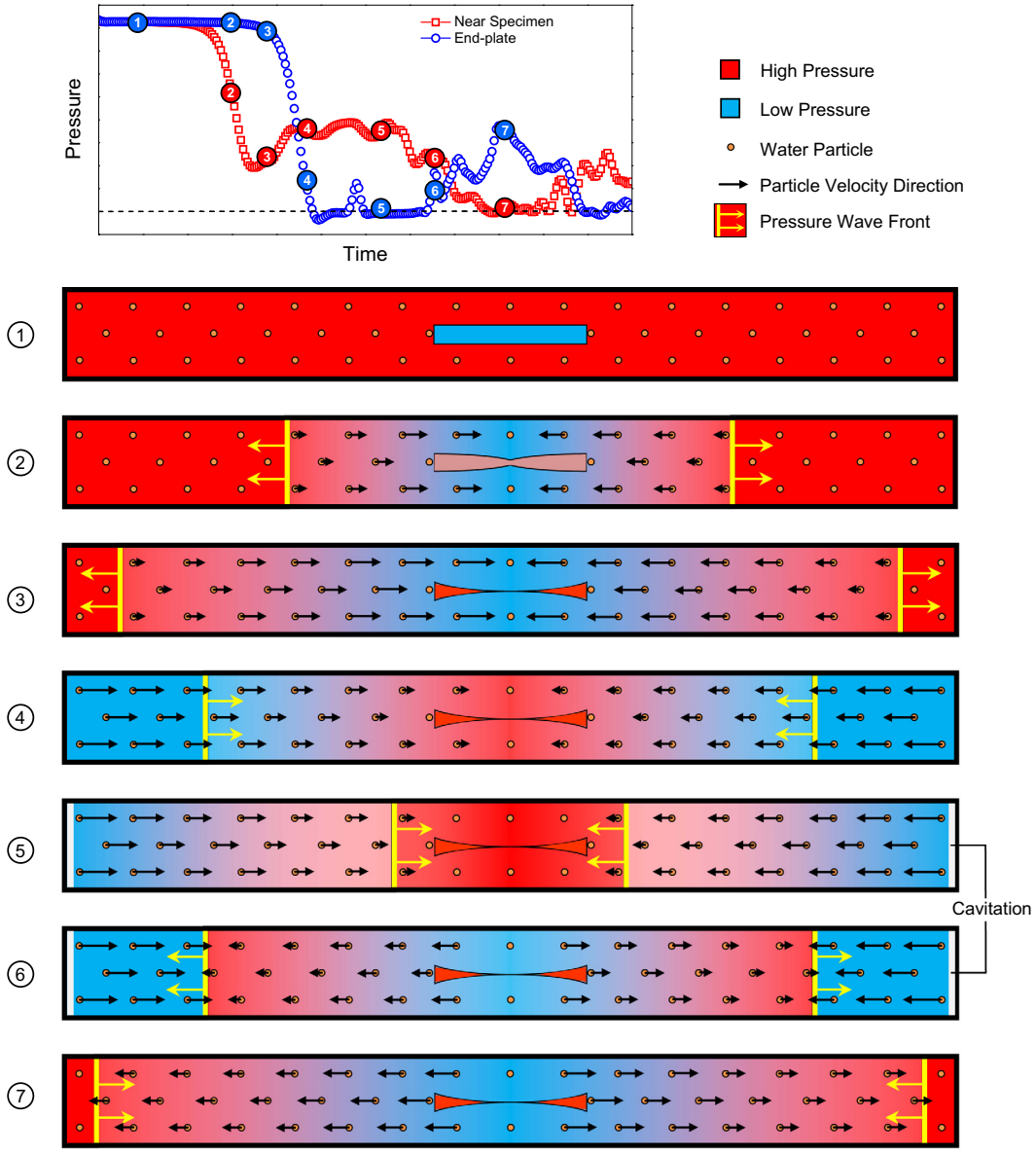

Fig. 7. Schematic of implosion process in the confining tube.

indicating the initiation of specimen wall contact. The magnitude of the pressure spike is approximately 0.82 MPa with the time duration of 50 μs. The quick depletion of hydrostatic pressure inside the confining tube during the implosion process is responsible for inhibiting the generation of a large pressure spike (above the initial hydrostatic pressure). The large pressure spike would be a result of the high pressure water rushing with high velocity against the walls of the implodable. In this case, the drop of hydrostatic pressure slows down the collapse process of the implodable. Thus, the surrounding low pressure water is incapable of generating a high pressure spike.

4.1.4. Pressure spatial distribution analysis

In order to better understand the axial pressure changes that take place, a plot of pressure in the confining tube as a function of transducer location is generated for different instants of time in Fig. 9 for all the geometries.

In the case of geometry 1, a local pressure drop at the center of the confining tube occurs and travels as an acoustic wave axially towards the end-plate as shown in Fig. 9(a). During the time that the local pressure at the center decreases towards its minimum, there is no change in the pressure away from the center. This pressure drop gradually develops almost as a normal distribution and by time $t = 1.8$ ms, it reaches the lowest pressure value of 1.1 MPa. At this instant, the implodable reaches the highest wall velocity relating to the highest decrease in pressure. After this point, the implodable begins to decelerate and wall contact occurs leading to a sudden velocity arrest and high deceleration in the wall movement. As a result, a compressive high pressure wave is emitted and an increase in pressure is seen at the center. Therefore a combination of an initial release wave and generation of compressive wave leads to a double valley shaped pressure distribution (see $t = 2.0$ ms and 2.1 ms in Fig. 9(a)).

For Geometry 2 and 3, the spatial gradients of pressure are decreased due to slower pressure decay rates providing enough time duration for pressure wave oscillation, and hence, an effective global hydrostatic pressure drop is observed. The rate of pressure drop at the center is slower for geometry 2 and 3, as compared to geometry 1, due to slower wall velocity of the implodable volumes (see Fig. 9(b) and (c)). As a result, the pressure release wave from the center reaches the end-plate at $t = 2.1$ ms for geometry 2, while still maintaining high pressure (2.25 MPa, 63% of the buckling pressure) at the center. It is also interesting to note that after the collapse process, the pressure at the center of the implodable reaches an approximate constant pressure state and does not decay further. This implies that the velocity of the implodable was really small and any pressure disturbances caused by the implodable can be ignored. The distribution of pressure for geometry 3 is very similar to geometry 2. The pressure wave evolution is even slower for geometry 3 with respect to geometry 2, leading to minimal pressure gradients.

4.1.5. Calculation of change in volume of the implodable as a function of time

Using the pressure histories obtained at different axial locations, two approaches can be utilized to estimate the change in volume of the implodable as a function of time (collapse progression): (1) Mean hydrostatic pressure approach, in which the change in the mean hydrostatic pressure inside the confining tube is directly proportional to the change in volume of implodable, (2) Water particle velocity approach, in which the cumulative inward flow of water towards the central region of the confining tube represents the change in volume of implodable.

4.1.5.1. Mean hydrostatic pressure approach. The implosion of cylindrical shells in a confined environment generates a local pressure drop as well as a global hydrostatic pressure drop across the entire confining tube. This mean hydrostatic pressure can be evaluated by spatially averaging the pressure at different axial locations and is plotted in Fig. 10(a). The initial pressure drop represents the collapse initiation in the specimens and this collapse progresses until the mean hydrostatic pressure reaches its first minimum value. For each case, it is evident from Fig. 10(a) that there is residual mean hydrostatic pressure wave present even after the end of collapse (>5 ms). This is due to: (1) pressure oscillations: elastic recovery and vibration of the specimen generates mean hydrostatic pressure pulses in the confining tube, and (2) residual pressure: a minimum critical pressure is required to progress the deformation of the specimen (Kyriakides and Babcock, 1981). If the mean pressure reaches below threshold value, no further deformation can be achieved. This phenomenon is similar to the 'propagation pressure in pipelines' reported earlier in the literature (Kyriakides and Babcock, 1981; Palmer and Martin, 1975; Dyau and Kyriakides, 1993).

In this analysis, the mean hydrostatic pressure is dominantly responsible for the deformation of the implodable. Also, the implodable is assumed to be in contact with water due to strong coupling between the water velocity and the implodable's wall velocity throughout collapse duration.

The inner volume of the confining tube ($V_{confining}$) at a mean hydrostatic pressure $P_m(t)$, and the volume of water (V_{water}) at any time t can be written as,

$$V_{\text{confining}} = \pi R^2 L\left(1 + \frac{P_m(t)R}{2\text{hE}}(5 - 4v)\right);$$
$$V_{\text{water}} = V_{\text{water\_i}}\left(1 + \frac{(P_c - P_m(t))}{K}\right) \tag{7}$$

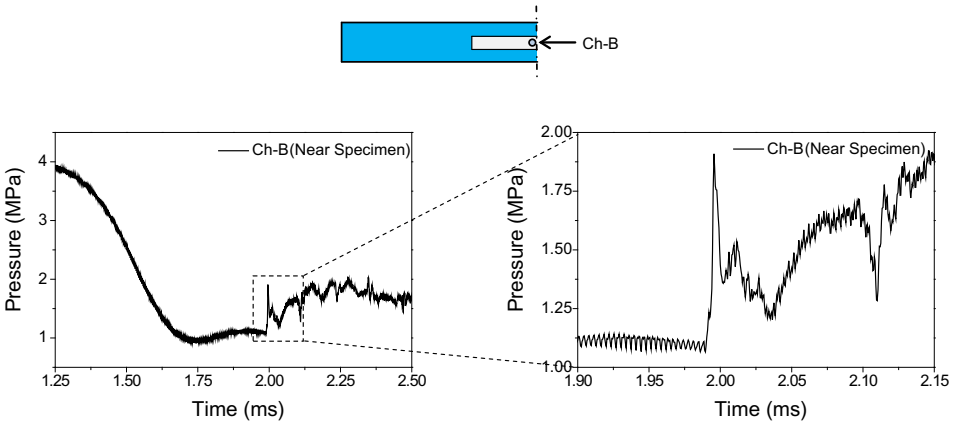

Fig. 8. Pressure spike observed in geometry 1 (31.8 mm OD).

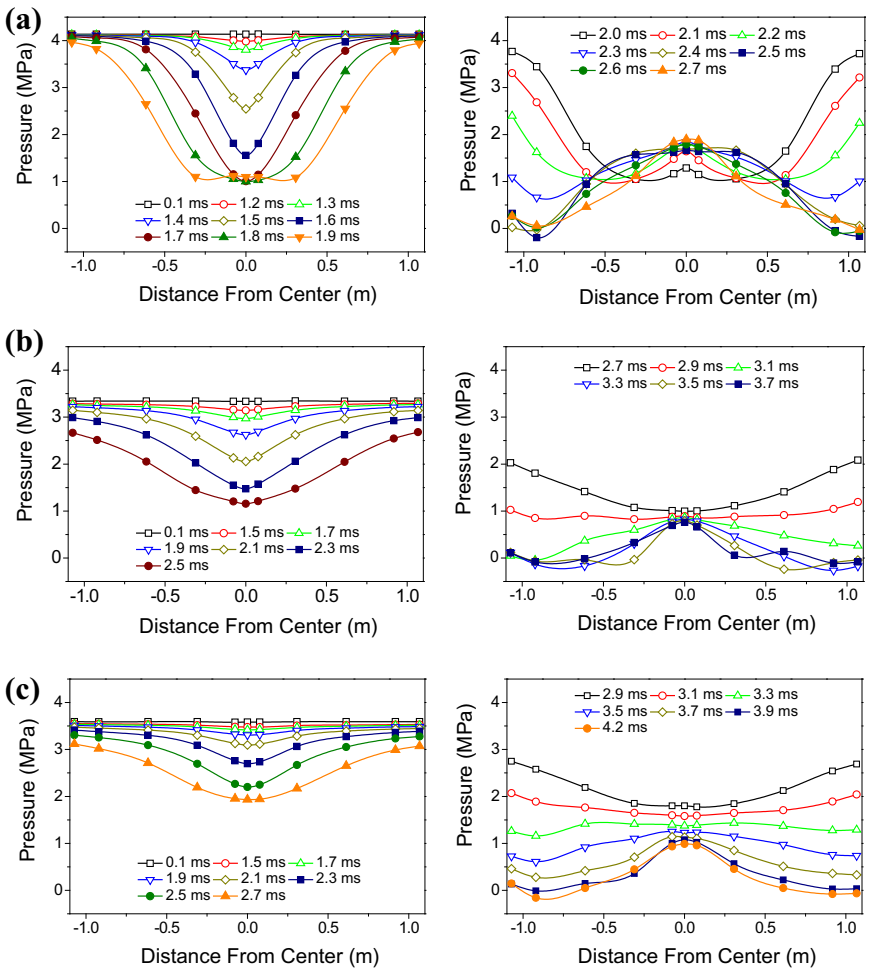

Fig. 9. Spatial distribution of pressure in the confining tube. (a) 31.8 mm OD implodable (geometry 1), (b) 50.8 mm OD implodable (geometry 2), and (c) 76.2 mm OD implodable (geometry 3).

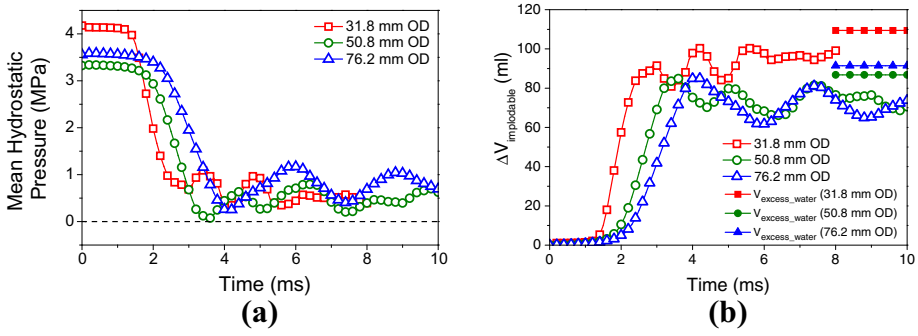

Fig. 10. (a) Mean hydrostatic pressure in the confining tube as a function of time, and (b) $\Delta V_{implodable}$ as a function of time using mean hydrostatic pressure approach.

Using $V_{water} + V_{implodable} = V_{confining}$,

$$V_{implodable} = \left[\pi R^2 L\left(1 + \frac{P_m(t)R}{2hE}(5-4\nu)\right)\right] - \left[V_{water\_i}\left(1 + \frac{(P_c - P_m(t))}{K}\right)\right] \quad (8)$$

The change in the volume of specimen ($\Delta V_{implodable}$) can be written as a function of mean hydrostatic pressure

$$\Delta V_{implodable} = V_{implodable\_i} - V_{implodable} = (P_c - P_m(t))\left[\pi R^2 L\left(\frac{1}{K} + \frac{R}{2hE}(5-4\nu)\right) - \frac{V_{implodable\_i}}{K}\right] \quad (9)$$

Using Eq. (9), the decrease in the volume of implodable as a function of time is plotted in Fig. 10(b). It can be seen that the change in volume of implodable for geometry 1, 2 and 3 is approximately 96 ml, 76 ml and 71 ml respectively. It is striking that the smallest

implodable exhibits the largest change in volume during implosion, while largest implodable exhibits the smallest change in volume. The reason being is that the extent of deformation (or $\Delta V_{implodable}$) depends upon V_{excess_water} present in the confining tube rather than the size of the implodable itself. Since $V_{excess\_water} \propto P_c$ from Eq. (5), it implies that the extent of deformation will increase with increasing buckling pressure.

The V_{excess_water} in the confining tube for geometry 1, 2 and 3 respectively is ~109 ml, 87 ml and 91 ml (from Eq. (5)) and it is represented by the solid symbol in Fig. 10(b). It can be seen that a higher amount of V_{excess_water} leads to a higher $\Delta V_{implodable}$ during implosion and the difference between V_{excess_water} present in the system and $\Delta V_{implodable}$ for each experiment was approximately ~10–20% of V_{excess_water} . That there is a finite volume of V_{excess_water} present in the system after the collapse of the implodable is arrested indicates that there is a certain threshold of positive hydrostatic pressure below which the implosion process cannot continue. The difference between the V_{excess_water} and $\Delta V_{implodable}$ at the end of the event is discussed by Kyriakides and Babcock as the ratio of propagation pressure and critical buckling pressure (Kyriakides and Babcock, 1981). It concludes that the hydrostatic pressure cannot lead to positive work on the implodable, unless the mean hydrostatic pressure in the confining tube is larger than the propagation pressure (pressure required to continue the implosion process).

It is also interesting to note that the ratio of change in volume of implodable to the initial volume is significantly large for smaller implodable (~50%). This indicates that the small implodable is more likely to exhibit contact during implosion and this is consistent with the discussion in Section 4.1.3 that geometry 1 did exhibit wall contact.

4.1.5.2. Water particle velocity approach. The implosion process occurring at the center of the confining tube can be considered as a sink of water where a net inward flow of water is generated during the collapse process. The volume of net flow of water towards the center is approximately equal to the deformation of the implodable. Hence, this approach for the calculation of $\Delta V_{implodable}$ relies on the estimation of axial particle velocity of water inside the confining tube using appropriate fluid mechanics field equations.

The following equations represent the generalized equations of conservation of mass and momentum used in fluid mechanics,

$$\frac{\partial \rho}{\partial t} + \bar{u} \cdot \nabla \rho + \rho(\nabla \cdot \bar{u}) = 0 \tag{10}$$

$$\rho\left(\frac{\partial \bar{u}}{\partial t} + u \cdot \nabla u\right) = -\nabla P \tag{11}$$

where ρ is the density of the water, P is the pressure in water and $\bar{u}$ represents the flow field of the water in Eulerian coordinates. Using the pressure-density relationship,

$$\frac{\partial P}{\partial t} = \left(\frac{\partial P}{\partial \rho}\right)_{\rho=\rho_0} \frac{\partial \rho}{\partial t} \tag{12}$$

Eqs. (10) and (11) can be simplified as

$$\frac{1}{c_0^2}\left(\frac{\partial P}{\partial t} + \bar{u} \cdot \nabla P\right) + \rho(\nabla \cdot \bar{u}) = 0 \tag{13}$$

$$\rho_0\left(\frac{\partial \bar{u}}{\partial t} + \bar{u} \cdot \nabla \bar{u}\right) + \nabla P = 0 \tag{14}$$

where $c_0 = \sqrt{\left(\frac{\partial P}{\partial \rho}\right)_{\rho=\rho_0}}$ is the wave speed in water at atmospheric pressure and temperature. Although the flow of water at the center of the confining tube is a combination of inward radial and axial flow, the axial wave assumption is valid beyond the unsupported length of the implodable (See 'dotted' region in Fig. 11, $|x| > l/2$). Therefore the conservation equations can be further written as

$$\frac{1}{c_0^2}\left(\frac{\partial P}{\partial t} + u\frac{\partial P}{\partial x}\right) + \rho\frac{\partial u}{\partial x} = 0 \tag{15}$$

$$\rho\left(\frac{\partial u}{\partial t} + u\frac{\partial u}{\partial x}\right) + \frac{\partial P}{\partial x} = 0 \tag{16}$$

where x is the axis of the confining tube with the center at the origin and u represents the velocity of water in the x -direction. If the volumetric flow rate of water crossing boundaries PQ and RS (in Fig. 11) towards the center is estimated, the accumulation of water ($\Delta V_{implodable}$) can be calculated as a function of time. Please note that in this approach, the compressibility of water in the central region is ignored and all the water crossing the boundary PQ and RS is considered to be preserving its volume.

These governing equations, Eqs. (15) and (16), couple the spatial distribution and time evolution of pressure ($P(x,t)$) as well as the fluid particle velocity ($u(x,t)$). Using the experimentally obtained pressure histories at different axial locations, a complete description of $P(x,t)$ can be estimated. Hence, the spatial pressure gradient $\frac{\partial P}{\partial x}(x,t)$ and pressure change rate $\frac{\partial P}{\partial t}(x,t)$ can be obtained by differentiation of $P(x,t)$. But, the coupled nature of these equations lead to high coupling between $\frac{\partial P}{\partial t}$, $\frac{\partial P}{\partial x}$, u, $\frac{\partial u}{\partial x}$ and $\frac{\partial u}{\partial t}$. This implies that $u(x,t)$ cannot be explicitly calculated from these equations easily. Therefore, $\frac{\partial u}{\partial t}$ is represented in terms of $\frac{\partial P}{\partial x}$, $\frac{\partial P}{\partial t}$ and u by following steps:

$$\rho\left(\frac{\partial u}{\partial t} + u\frac{\partial u}{\partial x}\right) + \frac{\partial P}{\partial x} = 0 \tag{17}$$

$$\Rightarrow \rho\frac{\partial u}{\partial t} + u\left[-\frac{1}{c_0^2}\left(\frac{\partial P}{\partial t} + u\frac{\partial P}{\partial x}\right)\right] + \frac{\partial P}{\partial x} = 0 \quad \text{(Using Eq.(15))} \tag{18}$$

$$\Rightarrow \rho\frac{\partial u}{\partial t} + \frac{\partial P}{\partial x}\left(1 - \frac{u^2}{c_0^2}\right) - \frac{u}{c_0^2}\frac{\partial P}{\partial t} = 0 \tag{19}$$

As the water particle velocity is very small as compared to the wave speed in water during the implosion process ($u \sim 25$–50 m/s $\Rightarrow u/c_0 \ll 1$), Eq. (19) can be rewritten as,

$$\Rightarrow \rho\frac{\partial u}{\partial t} = \frac{u}{c_0^2}\frac{\partial P}{\partial t} - \frac{\partial P}{\partial x} \tag{20}$$

The plot of $\frac{\partial P}{\partial x}$ and $\frac{\partial P}{\partial t}$ obtained at different times as a function of axial location is shown in Fig. 12.

The spatial pressure gradient ($\frac{\partial P}{\partial x}$) exhibits the highest value of 7 MPa/m for the case of geometry 1, while other geometries exhibit relatively smaller $\frac{\partial P}{\partial x}$ of 2.5 MPa/m and 1.9 MPa/m for geometry 2 and 3 respectively. The pressure gradients for geometry 1 develop quickly and propagate as a wave towards the ends of the confining tube, while the other two geometries exhibit slow development, leading to reflections from the ends.

Similar to $\frac{\partial P}{\partial x}$, the pressure decay rate ($\frac{\partial P}{\partial t}$) at the center also exhibits the highest value of 9 GPa/s for geometry 1, while both geometry 2 and 3 show $\frac{\partial P}{\partial t}$ of ~3 GPa/s and 2.5 GPa/s. The slow $\frac{\partial P}{\partial t}$ for geometry 2 and 3 is a direct indication of slow collapse progression. At the end-plates, the maximum $\frac{\partial P}{\partial t}$ was ~13 GPa/s, 5 GPa/s and 4 GPa/s for geometry 1, 2 and 3 respectively, which is almost twice the magnitude encountered in each case at the center indicating rigid reflection of pressure wave at the end-plates discussed in Section 4.1.2 (Taylor, 1963).

Using the following initial conditions (Eq. (21)) for Eq. (20), the water velocity $u(x,t)$ at different axial locations as a function of time can be obtained by iteratively solving for u in Eq. (18) using a finite difference scheme.

$$u(x, t=0) = 0; \quad P(x, t=0) = P_c \tag{21}$$

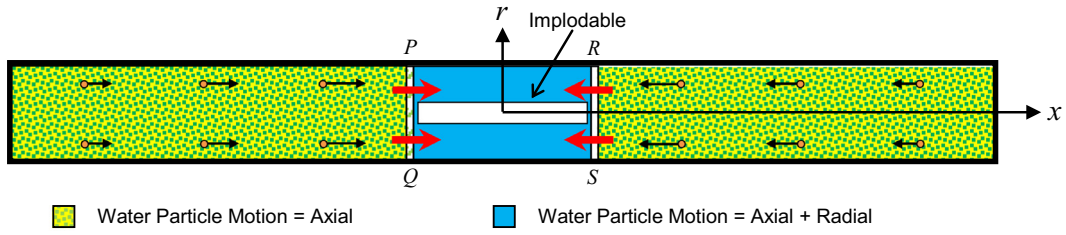

Fig. 11. Region of axial wave assumption in the confining tube.

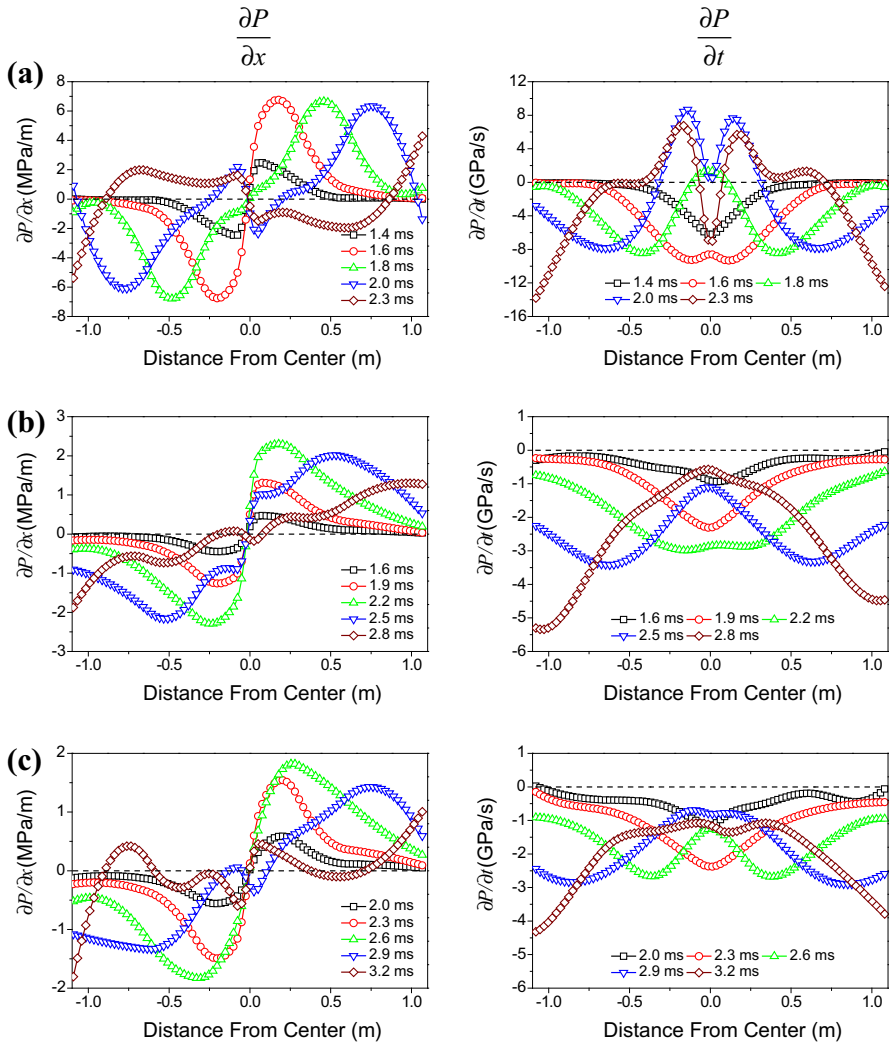

Fig. 12. Spatial distribution of $\frac{\partial P}{\partial x}$ and $\frac{\partial P}{\partial t}$ in the confining tube. (a) 31.8 mm OD implodable (geometry 1), (b) 50.8 mm OD implodable (geometry 2), and (c) 76.2 mm OD implodable (geometry 3).

This approach for estimating $u(x,t)$ is simple, as it only utilizes initial conditions of the problem and no boundary conditions are required at the end-plates. It eliminates the issue of characterizing the complex boundary condition present at the end-plate (stress-free boundary condition after cavitation, zero-velocity rigid boundary condition otherwise). The time histories of water velocity for the three geometries at different axial locations are plotted in Fig. 13. This figure shows the maximum water velocity (*PQ*/*RS*, From Fig. 11) achieved for geometry 1 is 2.2 m/s (at 1.85 ms), while it is 1.69 m/s (at 2.9 ms) for geometry 2 and 1.32 m/s (at 3.37 ms) for geometry 3. The total volumetric flow rate of water accumulated in *PQRS* region or $\Delta V_{implodable}$ can be written as

$$\Delta V_{implodable}(t) \approx \int_0^t \left[(|u_{PQ}| + |u_{RS}|) \times \frac{\pi}{4}(D^2 - d^2) \right] dt \tag{22}$$

where $|u_{PQ}|$and$|u_{RS}|$ represent the magnitude of water velocity at location *PQ* and *RS* respectively. The plot of $\Delta V_{implodable}$ as a function of time is shown in Fig. 14. It can be seen that the estimation of $\Delta V_{implodable}$ from water velocity approach is similar to mean hydrostatic pressure approach as shown in Fig. 10(b).

4.1.6. Transient collapse model for predicting complete deformation history of cylindrical shells

During the progression of the collapse of a cylindrical shell prior to wall contact, there is a specific mode associated with an initial

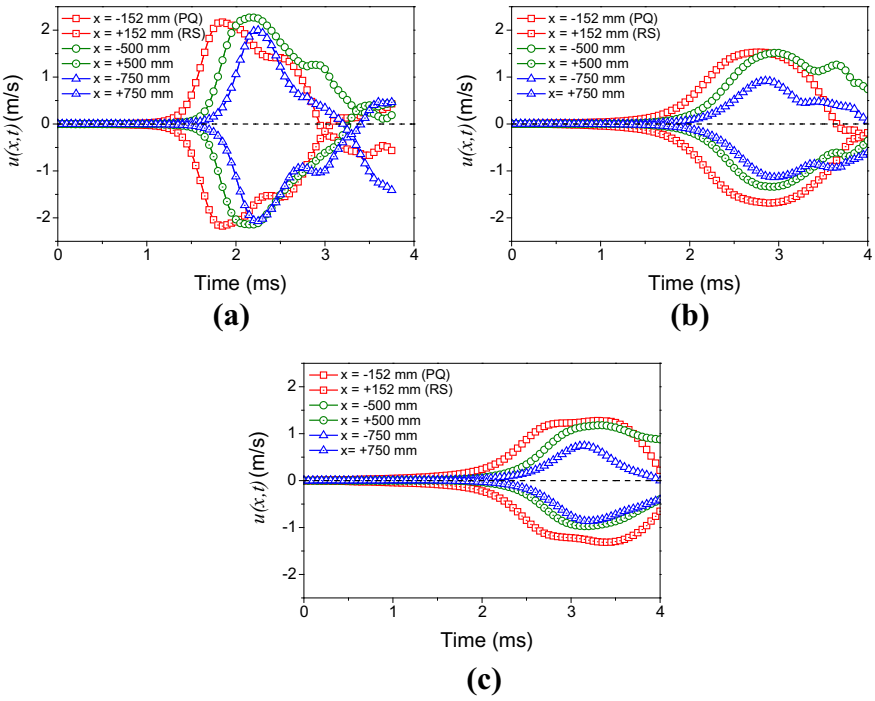

Fig. 13. Water velocity $u(x,t)$ as a function of time. (a) 31.8 mm OD implodable (geometry 1), (b) 50.8 mm OD implodable (geometry 2), and (c) 76.2 mm OD implodable (geometry 3).

given geometry. This collapse mode primarily defines the deformation of the shell during collapse process (note that the high order non-volume preserving vibration modes have been ignored). Hence, the extent of collapse ($\Delta V_{implodable}$) in cylindrical shells can be expressed as a function of the deformation at a single point (r_1, θ_1, z_1) (the mid-point in this case) on the shell uniquely for a specific geometry.

$$\Delta V_{implodable}(t) = f\left(\bar{U}(r_1, \theta_1, z_1, t)\right) \tag{23}$$

This deformation model is generally a nonlinear function for a specific geometry hence it is numerically evaluated in this study for all the geometries. A dynamic buckling simulation of the implodables (without fluid) chosen in this study was performed using DYSMAS and the internal volume of the implodables was estimated as a function of mid-point displacement. A typical deformation model calculated is shown in Fig. 15(a), in which $\Delta V_{implodable}$ for all the geometries used in this study is expressed as a function of mid-point displacement. It is noted from Fig. 15(a) that for both 31.8 mm and 50.8 mm OD, the initial change in volume can be approximately represented as a quadratic function of mid-point displacement. It is interesting to note that the $\Delta V_{implodable}$ observed for 50.8 mm OD has a very similar trend as the 31.8 mm OD up to ~16 mm displacement. As $\Delta V_{implodable}$ has been shown to be estimated by both mean hydrostatic pressure approach and water particle velocity approach, the mid-point deformation of the implodable can be back calculated using this deformation model ($\bar{U}(r_1, \theta_1, z_1, t) = f^{-1}(\Delta V_{implodable}(t))$). This model is further used to predict the time evolution of mid-point velocity of the implodable and is shown in Fig. 15(b). It is clear that the maximum velocity achieved during implosion is largest for geometry 1 (~25 m/s). Geometry 1 also exhibits the largest accelerations, which is characteristic of sudden collapse of a structure. On the contrary, geometry 2 exhibits a smaller maximum velocity of 12 m/s and ~5 times slower accelerations. Hence, it can be inferred that the implosion of larger geometries in a confining space is a slow process and the velocities achieved in such cases are much smaller as compared to a free-field natural implosion.

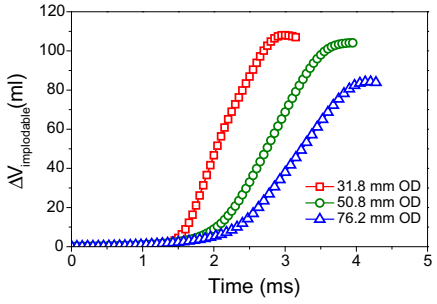

Fig. 14. $\Delta V_{implodable}$ as a function of time for all geometries from water velocity approach.

It should be noted that the transient deformation model for geometry 3 is not discussed here because it did not exhibit the evolution of mode-2 collapse and just an indentation was observed during the confined tube implosion experiments.

4.1.7. Redistribution of energy in the confining tube

In the implosion experiments conducted inside a confining tube, the total energy of the whole system, i.e. confining tube + water + implodable + air inside implodable, should be constant during the collapse process because the system is isolated and there is no flow of energy from outside in the system. Therefore, the energy balance between the initial state (prior to the onset of implosion) and at any time $t = t_1$ can be written as,

$$E_{t=0} = E_{t=t_1} + E_{loss} \tag{24}$$

$$E_{confining}\big|_{t=0} + E_{water}\big|_{t=0} = E_{confining}\big|_{t=t_1} + E_{water}\big|_{t=t_1} + E_{implodable}\big|_{t=t_1} + E_{air}\big|_{t=t_1} + E_{loss} \tag{25}$$

It can be noted in Eq. (25) that the initial energy terms for the implodable and the air have been omitted because at the onset of the implosion process, there is no significant deformation in the

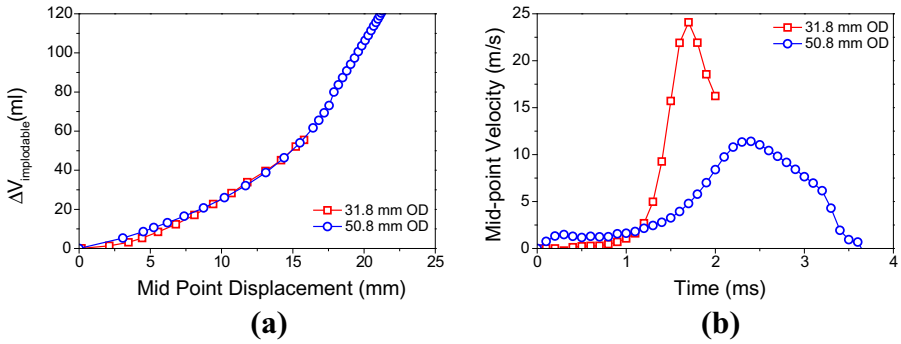

Fig. 15. (a) $\Delta V_{implodable}$ as function of mid-point deflection, and (b) calculated mid-point velocity of implodable.

implodable causing no change in these energies. Different energies present in the water and structure can be estimated as follows:

- The energy in the confining tube

$$E_{confining}\big|_{t=t_1} = \frac{1}{2}(\sigma_{\theta\theta}\varepsilon_{\theta\theta} + \sigma_{xx}\varepsilon_{xx})V_{confining\_shell} = \frac{\pi R^3 P_m(t_1)^2 L}{Eh}\left[\frac{5}{4} - \nu\right] \tag{26}$$

  where σ_{xx} = axial stress; ε_{xx} = axial strain; $\sigma_{\theta\theta}$ = hoop stress; $\varepsilon_{\theta\theta}$ = hoop strain; $V_{confining\_shell}$ = volume of confining tube material.
- The energy in the water

$$E_{water}\big|_{t=t_1} = Potential\ Energy\ (P.E._{\cdot water}) + Kinetic\ Energy\ (K.E._{\cdot water})$$
$$P.E._{\cdot water}\big|_{t=t_1} = \frac{\pi R^2 L P_m(t_1)^2}{2K};\quad K.E._{\cdot water}\big|_{t=t_1} = \frac{\rho\pi R^2 L}{2}u_{rms}^2(t_1) \tag{27}$$

  where $u_{rms}(t_1)$ = root mean square velocity inside the confining tube = $\left[\frac{1}{L}\int_{-L/2}^{L/2} u^2(x,t_1)dx\right]^{1/2}$
- The energy absorbed in elasto-plastic deformation of implodable: This energy is taken to be the strain energy absorbed through elasto-plastic deformation of the implodable's walls during collapse. This strain energy of the cylinder walls is output explicitly from the DYSMAS simulation throughout time and it is estimated by the volume integration of the strain energy per unit volume. A detailed discussion of the calculation of the strain energy in the walls of an implodable during collapse is provided by Chamberlin and Guzas (2012). $E_{implodable}$ calculated from DYSMAS was investigated as a function of mid-point displacement and the calculations of mid-point displacement shown in Section 4.1.6 was used to track the $E_{implodable}$ as a function of time.
- The energy present in air

$$E_{air}\big|_{t=t_1} = P_{atm}V_{specimen\_i\_air}^{\gamma}\left[\frac{V_{specimen\_air}^{1-\gamma}(t_1) - V_{specimen\_i\_air}^{1-\gamma}}{1-\gamma}\right] \tag{28}$$

  $V_{specimen\_i\_air}$ = volume of air inside specimen before implosion $t = t_1$
  $V_{specimen\_air}(t_1)$ = volume of air inside specimen at time
  P_{atm} = atmospheric pressure = 0.101 MPa
  γ = adiabatic index for air = 1.4
- Although the confining space in the tube is highly energy efficient, energy losses are present in the system and these include viscous losses, phase change/cavitation energy loss, and frictional losses in the implodable at wall contact and at end caps of implodable.

The plot of all these energies as a function of time for geometries 1 and 2 is shown in Fig. 16. It is evident from Fig. 16 that the initial hydrostatic potential energy decays rapidly during the implosion process. A major part of initial hydrostatic potential energy in water transforms into the work done in the elasto-plastic deformation of the implodable and the kinetic energy of the water. The rapid collapse of geometry 1 leads to large movement of water causing high kinetic energy in the water (~ 90 J), while the slow collapse of geometry 2 leads to small kinetic energy in the water (~ 42 J). Still in both of the cases, it was seen that a significant portion of the initial hydrostatic potential energy transforms into the elasto-plastic deformation of the implodable. In these experiments, the energy going into the adiabatic compression of the air inside the implodable and the elastic energy contribution from the confining tube as shown in Fig. 16 is found to be very small as compared to other energies. The calculation of E_{loss} using Eq. (25) also shows that there is relatively small energy loss (7–13%) at the end of the implosion process.

With the combination of velocity of the implodable and the energy redistribution, it can be established that there are two types of implosions that could occur within a confining tube: (1) rapid implosion and (2) slow/partial implosion. Rapid implosion occurs when the energy available in the confining environment is much larger as compared to plastic dissipation energy of a completely collapsed implodable. These implosions are characterized by rapid energy transfer from surrounding water to the implodable, which also leads to significant transfer of energy into kinetic energy of water (~50%). On the contrary, slow implosion occurs when the energy available in the confining environment is smaller than the plastic dissipation energy of a collapsed implodable. In this case, most of the potential energy available transfers into plastic dissipation in the implodable leading to negligible transfer into kinetic energy of water (<20%). With this approach, a new deformation model can be formulated where the deformation of the implodable for slow implosion can be approximated by the energy balance between the loss of hydrostatic potential energy and the gain in total deformation energy (elastic and plastic) of the implodable. This methodology holds accurate until the kinetic energy gained during implosion is not negligible as compared to initial hydrostatic potential energy.

4.2. Comparison of computational results

The computational models that have been developed for each of the respective implodable geometries are correlated to the experimental results utilizing available experimental data, specifically the pressure time histories and final collapsed shapes of the specimens. Additionally, based on acceptable correlation between the experimental data and simulation results, further observations are made consisting of the pressure fields in the full fluid domain and the collapse progression of the implodables.

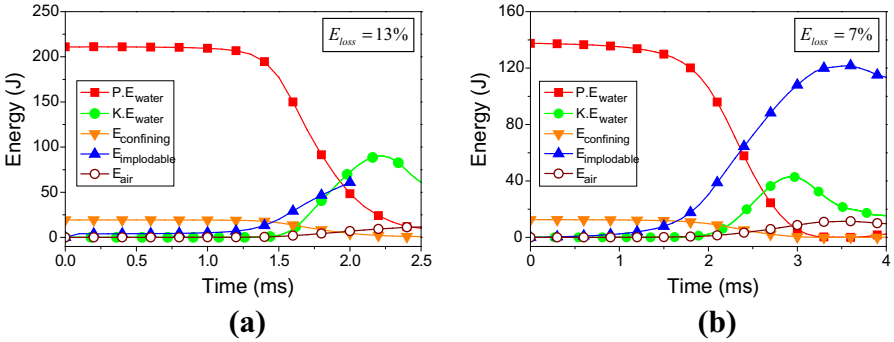

Fig. 16. Energy redistribution inside confining tube. (a) 31.8 mm OD implodable (geometry 1), and (b) 50.8 mm OD implodable (geometry 2).

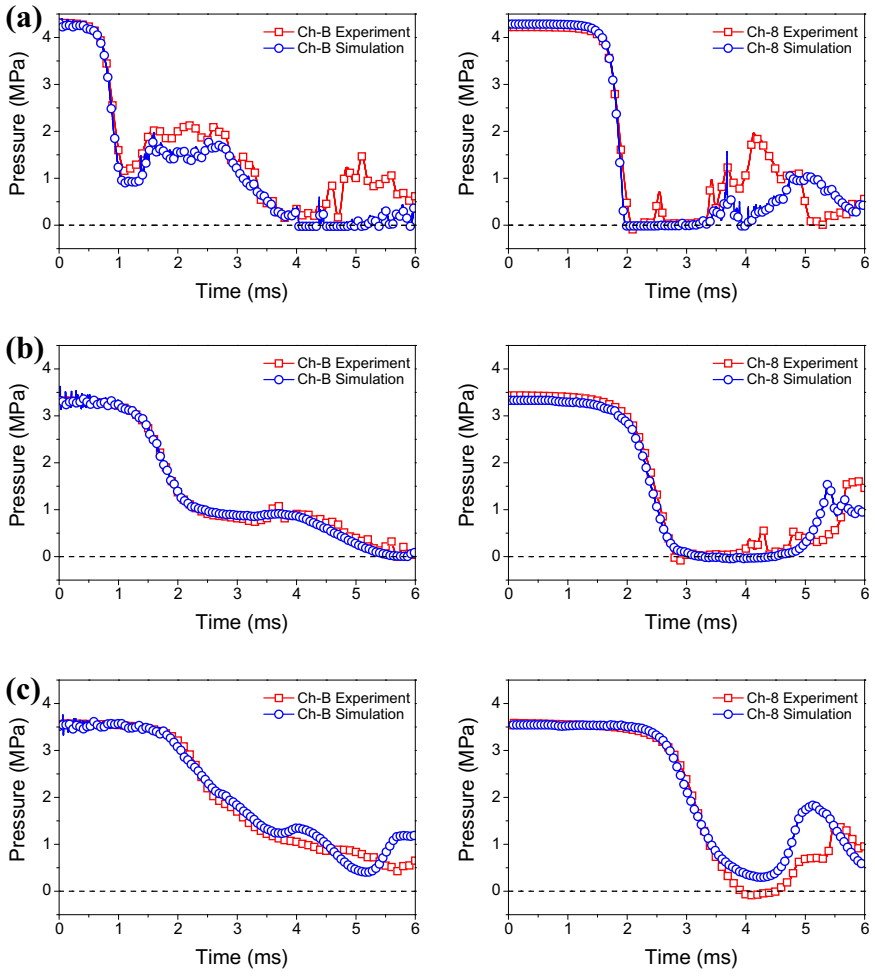

Fig. 17. Comparisons of experimental and numerical pressure histories in the confining tube. (a) 31.8 mm OD implodable (geometry 1), (b) 50.8 mm OD implodable (geometry 2), and (c) 76.2 mm OD implodable (geometry 3).

Comparisons of the experimental and computational pressure histories for the centerline gage (ch-B) and the end cap gage (ch-8) are provided in Fig. 17. From these figures it is seen that at both the centerline and the end cap locations there is good agreement between the simulations and the experiments. Specifically the computational models accurately predict both the rate of pressure drop during the implosion as well as the magnitude of the drop. Furthermore, the simulations are able to predict the onset, and time duration, of cavitation occurring at the end caps of the confining tube as indicated by the zero pressure region in the ch-8 figures. The models also predict the development of a pressure pulse occurring at the end caps subsequent to the cavitation development, although in the simulation results the pressure pulse does occur at slightly different points in time as compared to the corresponding experiment with the 31.8 mm and the 50.8 mm showing a delayed pressure development and the 76.2 mm simulation predicting an earlier development. Similar levels of correlation are seen for all pressure gage comparisons (ch-2 to 4, ch-A) and are omitted for brevity in the current discussion.

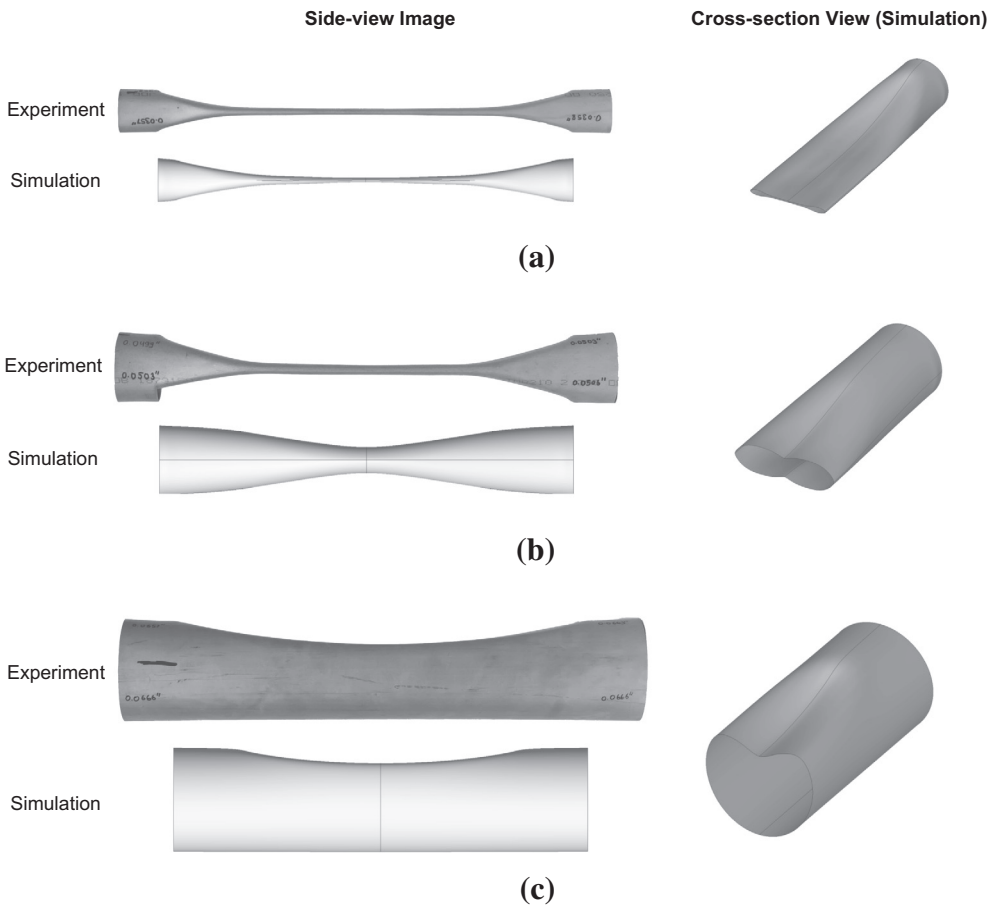

Fig. 18. Comparison of final collapse shape of the implodable. (a) 31.8 mm OD implodable (geometry 1), (b) 50.8 mm OD implodable (geometry 2), and (c) 76.2 mm OD implodable (geometry 3).

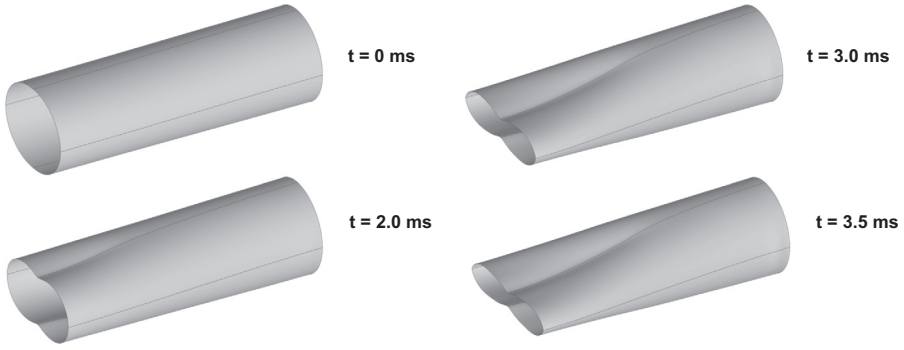

Fig. 19. Progression of collapse for 50.8 mm OD implodable from simulations.

Fig. 18 shows the comparison of collapsed shapes between the experiments and the simulations. From the side-view figure comparison, it is seen that the computational models are able to accurately capture the mode shape of the collapse but the extents of the collapse progression for computational simulations are slightly smaller as compared to the experimental results. This is because of the later effects (>10 ms) of the pressurization (due to the pump running for a finite amount of time after the implosion), which leads to minor additional collapse of the implodable during experiments.

Specifically, the models predict a mode-2 collapse for all models with the 31.8 mm geometry collapse progressing nearly the full length of the implodable, which agrees well with the experimental results. By comparison the 50.8 mm geometry does not fully collapse in the simulation and the collapse is arrested prior to the opposing walls impacting each other. Finally, although the 76.2 mm implodable does initially begin to collapse, due to the effects of the hydrostatic pressure, the collapse only begins on one side of the implodable and is arrested prior to the opposite side obtaining any inward motion. This is likely due to a sufficiently rapid drop in surrounding pressure that the driving force of the implosion is quickly removed. Similar one side collapse for 76.2 mm was observed in experimental results.

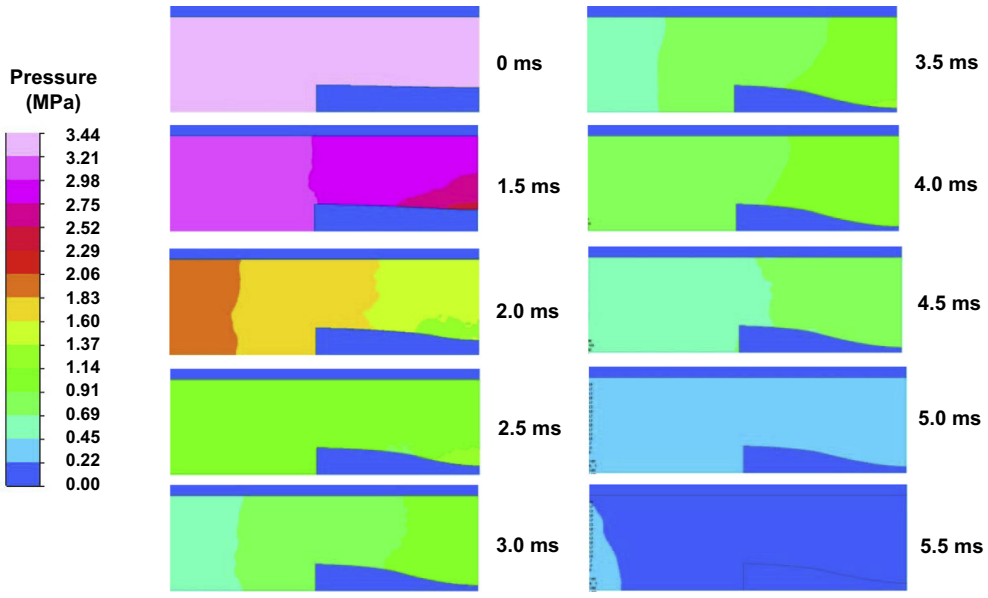

Fig. 20. Fluid pressure contours inside confining tube for 50.8 mm OD implodable volume from simulations.

Cross sectional views of the final collapsed shape for each implodable are also provided in Fig. 18 which show the relative progression inward of the centerline of the volumes.

In order to verify the predictions of analytical models proposed in Section 4.1.5.1, a comparison between analytically and numerically evaluated $\Delta V_{implodable}$ is performed. It is seen that the value of $\Delta V_{implodable}$ from numerical simulations is ~92 ml and 70 ml for geometry 1 and 2 respectively, while analytical calculations predict ~96 ml (4% difference) and 76 ml (8.5% difference) for the corresponding geometries. Hence, it can be concluded that the proposed analytical approaches can accurately predict the extent of deformation in confined implosion processes.

Figs. 19 and 20 show the collapse progression and resulting fluid field pressure contours for the 50.8 mm implodable simulation. From the structural collapse evolution it is seen that although the implosion is initiated by indenting the top surface of the structure, the structural instability quickly causes both sides to gain radially inward motion as expected. For the case of both the 50.8 and 76.2 mm implodable this inwards motion is ultimately arrested prior to the opposing surfaces impacting at the horizontal plane. From Fig. 20, it is seen that when the implosion is initiated and the walls begin to move inwards there is an associated drop in surrounding fluid pressure. This pressure drop begins at the axial plane of symmetry and then progresses towards the end cap in a form of a release wave as water rushes towards the center to fill the void resulting from the inward motion of the implodable walls. This axial progression of the pressure drop is also displayed in the time histories in that there is a time delay between the initial pressure drop at the center gage and the pressure drop at the end cap gage. Since there is a fixed volume of water within the confining tube and there is no available reservoir of fluid to maintain the hydrostatic pressure in the system, there is also a net decrease in the hydrostatic pressure of the surrounding fluid. It is this hydrostatic pressure which is required to continue driving the collapse of the implodable, and when this driving force drops below a certain critical level the implosion will be arrested. From the pressure field contours of 5 and 5.5 ms, it is seen that the net hydrostatic pressure in the fluid body is approximately less than 0.45 MPa (less than 15% of the initial collapse pressure of 3.44 MPa).

5. Conclusions

An experimental study along with computational simulations was conducted to understand the implosion mechanics inside a confining environment. The key findings of this study are as follows:

(1) The limited energy present inside the confining tube significantly influences the implosion process. The normalized extent of collapse (i.e.$\Delta V_{implodable}/V_{implodable\_i}$) is larger for the small diameter implodable compared to larger implodable volumes. In each case, the change in volume of the implodable ($\Delta V_{implodable}$) is approximately 80–90% of the excess compressible water present inside the confining tube.

(2) Pressure history inside the confining tube can be described as (a) a local decrease in pressure near the implodable, generating a pressure release wave traveling outwards to the end-plates. (b) The release wave rapidly decreases the pressure at the end-plates to zero-pressure, while the pressure is maintained at the center. (c) The high pressure wave generated at the center hits the end-plates leading to high pressure hammer wave.

(3) The pressure gradients and the pressure decay rate decrease within the confining tube with increasing implodable diameter. In turn, the average axial particle velocity of water inside the confining tube decreases with increasing diameter implodable.

(4) The initial potential energy present in the water transforms into two parts: (a) elasto-plastic work done on the implodable and (b) kinetic energy in the water. The small diameter implodable exhibits rapid collapse process, while large implodable diameters exhibit slower collapse. This results into higher kinetic energy in water during the implosion of small implodable diameters as compared to large diameter implodables.

(5) Computational simulations using coupled Eulerian–Lagrangian approach can accurately predict the pressure histories as well as the collapse progression of a confined implosion event. The evolution of implosion process, the resulting fluid motion, the pressure waves' generation, and the hammer wave are distinctly captured in the simulations.

Acknowledgements

The authors kindly acknowledge the financial support provided by the Office of Naval Research Computational Mechanics Program managed by Dr. Stephen E. Turner under Grant No. N00014-12-1-0382 (URI) and N0001412WX21206 (NUWC).

References

Bitter, N.P., Shepherd, J.E., 2014. Dynamic buckling and fluid–structure interaction of submerged tubular structures. In: Shukla, A., Rajapakse, Y.D.S., Hynes, M.E. (Eds.), Blast Mitigation - Experimental and Numerical Studies. Springer, New York, pp. 189–227.

LeBlanc, J.M., Ambrico, J.M., Turner, S.E., 2014. Underwater implosion mechanics: experimental and computational overview. In: Shukla, A., Rajapakse, Y.D.S., Hynes, M.E. (Eds.), Blast Mitigation - Experimental and Numerical Studies. Springer.

Budiansky, B., Hutchinson, J.W., 1966. A survey of some buckling problems. AIAA J. 4, 1505–1510.

Buthod, P., 1983. Pressure vessel handbook, sixth ed.

Cartlidge, E., 2001. Accident grounds neutrino lab.

Chamberlin, R.E., Guzas, E.L., 2012. Investigation of the Fundamental Drivers in Implosion Dynamics, 83rd Shock & Vibration Symposium, New Orleans, LA, November 4-8.

Charter, E., Hutchinson, J.W., Neale, K.W., 1983. Buckle propagation on a beam on a nonlinear elastic foundation. In: Proceedings IUTAM Symposium Collapse: The Buckling of Structures in Theory and Practice. Cambridge University Press, Cambridge, UK, pp. 31–41.

Costa, L.A., Turner, S.E., 2008. Implosion testing within a pipe, NUWC-NPT Technical Memo No. 08–014.

Dyau, J.Y., Kyriakides, S., 1993. On the propagation pressure of long cylindrical shells under external pressure. Int. J. Mech. Sci. 35 (8), 675–713. http://dx.doi.org/10.1016/0020-7403(93)90018-P.

Diwan, M., Dolph, J., Ling, J., Sharma, R., Sexton, K., Simos, N., Tanaka, H., Arnold, D., Tabor, P., Turner, S., 2012. Underwater implosions of large format photomultiplier tubes. Phys. Proc. 37, 715–721. http://dx.doi.org/10.1016/j.phpro.2012.03.721.

Farhat, C., Rallu, A., Shankaran, S., 2008. A higher-order generalized ghost fluid method for the poor for the three-dimensional two-phase flow computation of underwater implosions. J. Comput. Phys. 227, 7674–7700. http://dx.doi.org/10.1016/j.jcp.2008.04.032.

Farhat, C., Wang, K.G., Main, A., Kyriakides, S., Lee, L.-H., Ravi-Chandar, K., Belytschko, T., 2013. Dynamic implosion of underwater cylindrical shells: experiments and computations. Int. J. Solids Struct. 50, 2943–2961. http://dx.doi.org/10.1016/j.ijsolstr.2013.05.006.

Harben, P.E., Boro, C., 2001. Implosion source development and diego garcia reflections. In: 23rd Department of Defense/Department of Energy Seismic Research Review, Jackson Hole, Wyoming.

Ikeda, C.M., 2012. Fluid-structure interactions: implosions of shell structures and wave impact on a flat plate. University of Maryland, College Park, Maryland.

Isaacs, J.D., Maxwell, A.E., 1952. The ball-breaker; a deep water signalling device. J. Mar. Res 11, 63–68.

Joukowsky, N., 1900. Über den hydraulischen stoss in wasserleitungsrohren. St Petersburg Memoires L'AacademieImperiale Sci. 8th Ser. IX.

Kadioglu, S.Y., Sussman, M., 2008. Adaptive solution techniques for simulating underwater explosions and implosions. J. Comput. Phys. 227, 2083–2104. http://dx.doi.org/10.1016/j.jcp.2007.10.019.

Korteweg, D., 1878. Über die fortphlanzungsgeschwindigkeit des schalles in elastisches rohren. Annu. Rev. Phys. Chem. 241, 525–542.

Kyriakides, S., Babcock, C.D., 1981. Experimental determination of the propagation pressure of circular pipes. J. Press. Vessel Technol. 103, 328–336. http://dx.doi.org/10.1115/1.3263410.

Kyriakides, S., Corona, E., 2007. Mechanics of Offshore Pipelines. Buckling and Collapse, vol. 1. Elsevier.

Kyriakides, S., Netto, T., 2000. On the dynamics of propagating buckles in pipelines. Int. J. Solids Struct. 37, 6843–6867. http://dx.doi.org/10.1016/S0020-7683(99)00317-0.

Ling, J., Bishai, M., Diwan, M., Dolph, J., Kettell, S., Sexton, K., Sharma, R., Simos, N., Stewart, J., Tanaka, H., Viren, B., Arnold, D., Tabor, P., Turner, S., Benson, T., Wahl, D., Wendt, C., Hahn, A., Kaducak, M., Mantsch, P., Sundaram, S.K., 2013. Implosion chain reaction mitigation in underwater assemblies of photomultiplier tubes. Nucl. Instrum. Methods Phys. Res., Sect. Accel. Spectrom. Detect. Assoc. Equip. 729, 491–499. http://dx.doi.org/10.1016/j.nima.2013.07.056.

Mesloh, R.E., Sorenson, J.E., Atterbury, T.J., 1973. Buckling and offshore pipelines. Gas Mag. 49, 40–43.

Orr, M., Schoenberg, M., 1976. Acoustic signatures from deep water implosions of spherical cavities. J. Acoust. Soc. Am. 59, 1155–1159.

Palmer, A.C., Martin, J.H., 1975. Buckle propagation in submarine pipelines. Nature 254, 46–48. http://dx.doi.org/10.1038/254046a0.

Potter, M.C., Wiggert, D.C., Hondzo, M., 2002. Mechanics of Fluids. Brooks Cole/Thompson Learning, Pacific Grove, CA.

Rayleigh, Lord, 1917. On the pressure developed in a liquid during the collapse of a spherical cavity. Philos. Mag. Ser. 6 (34), 94–98. http://dx.doi.org/10.1080/14786440808635681.

Simitses, G.J., 1986. Buckling and postbuckling of imperfect cylindrical shells: a review. Appl. Mech. Rev. 39, 1517–1524. http://dx.doi.org/10.1115/1.3149506.

Taylor, G.I., 1963. The Scientific papers of Sir Geoffrey Ingram Taylor. In: Batchelor, G.K. (Ed.), Aerodynamics and the Mechanics of Projectiles and Explosions. Cambridge University Press, Cambridge, UK.

Tijsseling, A.S., 2007. Water hammer with fluid-structure interaction in thick-walled pipes. Comput. Struct. 85, 844–851. http://dx.doi.org/10.1016/j.compstruc.2007.01.008.

Timoshenko, S.P., Gere, J.M., 1963. Theory of elastic stability.

Turner, S.E., 2007. Underwater implosion of glass spheres. J. Acoust. Soc. Am. 121, 844–852.

Turner, S.E., Ambrico, J.M., 2012. Underwater implosion of cylindrical metal tubes. J. Appl. Mech. 80, 011013. http://dx.doi.org/10.1115/1.4006944.

Urick, R.J., 1963. Implosions as sources of underwater sound. J. Acoust. Soc. Am. 35, 2026–2027. http://dx.doi.org/10.1121/1.1918898.

Vath, F., Colletti, W., 1968. Development of buoyancy material for deep submergence search vehicle evaluation of sympathetic implosion of buoyancy modules. U.S Naval Applied Science Laboratory, Brooklyn, New York.

Von Mises, R., 1929. The critical external pressure of cylindrical tubes under uniform radial and axial load, pp. 418–430. (translated by D.F. Windenburg, S. Stodolas Festschr)